EMPS: Radiation Thermometer Designs

Howard W. Yoon, George P. Eppeldauer

1. Introduction

Since the publication of the “Theory and Practice of Radiation Thermometry” [1] in 1988, the designs of radiation thermometers have undergone drastic changes. With the exception of few industries, the disappearing filament pyrometers are not commonly used. The improvements in detector performance had led to an expansion of detector-based radiation thermometry where the temporally-stable response of the detector is needed to maintain the calibration. Also, the improvements in micro-bolometer array performance along with lower costs have led to inexpensive hand-held thermal imaging cameras for non-destructive testing and thermal diagnostic uses. Although thermal imagers can be calibrated for use as transfer standards, radiation thermometer designs with the lowest measurement uncertainties are obtained using spot-radiation thermometer designs which are capable of viewing the fixed-point blackbodies directly. In this chapter, the instrument design and characterizations of spot-radiation thermometers capable of transferring the temperature scales with the lowest uncertainties will be discussed. The radiation thermometers can be calibrated using the International Temperature Scale of 1990 (ITS-90) [[2]] or the radiation thermometers can be calibrated using absolute radiometry for thermodynamic temperature determinations. The chapter is also limited to radiation thermometers which operate in the visible[3] to the near-infrared[4] wavelength regions. The choice of the detector and optimization of the detector for stability and linearity will be discussed. The characterizations of radiation thermometers for size-of-source effect (SSE) will be discussed.

2. Design Considerations

The primary consideration in the design of a radiation thermometer is the desired range of operational temperatures. Fig. 1 shows the Planck radiances for blackbodies ranging in temperatures from the freezing temperature of In, or 430 K to 3000 K. Due to the non-linear relationship between radiance and temperature, the central wavelength of the radiation thermometer should be at shorter wavelengths than the peak wavelength of the Planck radiances for the temperature of interest. For the range of temperature from 150 °C to 962 °C (Ag freezing temperature) and for temperatures greater than 962 °C, the center wavelengths of the commonly used radiation thermometers are indicated by the two lines, respectively, at 1550 nm and at 650 nm. The separation of the temperature range of use is also important since the ITS-90 temperature traceability will be different for the two temperature ranges. If the temperature ranges are limited to those greater than 150 °C, then these considerations limit the types of detector materials and optical designs to those using Si or InGaAs diodes and also utilizing regular glass optics. It is important to also have low uncertainty photocurrent measurement systems or transimpedance current-to-voltage amplifiers since the proper design of the amplifiers is critical in obtaining linear, temporally stable photocurrent measurements for the lowest temperature uncertainties. The following sections discuss the optical designs of radiation thermometers the choice of the detectors, the choice of spectral filter, the current-to-voltage amplifier, and characterizations of spectral responsivity, linearity and SSE of radiation thermometers. Finally, calibrations of radiation thermometers for measurements of ITS-90 and thermodynamic temperatures are discussed.

3. Basic Optical Designs

Radiation thermometers typically will have either a reflective or a refractive lens to collect the radiation and to limit the field of view and the target size. As shown in Fig. 6, the simplest optical setup consists of an objective lens for collection which is integrated into a package with an aperture stop to focus the radiation onto a field stop which in turn limits the area of collection. If the analysis is limited to geometric optics, the field of view is simply the angle subtended by the diameter of the aperture stop and the object distance. The target area is the area of the field stop multiplied by the magnification factor of the object distance over the image distance. A spectral filter is placed between the collected radiation and the broad-band detector to limit the spectral transmittance. The spectrally selected radiation is incident on the photodiode producing the photo-induced current which is converted to voltage using a preamplifer. Each of these items in-turn will be discussed further in this chapter.

Another variation of the radiation thermometer is to have additional optics, as shown in Fig.3, to collimate or refocus the radiation after the field stop with additional lenses. These additional lenses enable the placement of the aperture stop after the field stop. In this design, the collimated radiation is transmitted through a large area on the spectral filter to reduce possible effect from spatial inhomogeneities of the filter. The impact of this design on the resulting SSE will be discussed later in this chapter.

Due to the developments in optical modeling software, the above simple designs are easily modeled using commercial software to determine, among many other optical properties, imaging quality such as the Strehl ratio, the effect of aberrations and chromatic focal shift. It is also possible to design custom lenses for the desired characteristics such as to improve the imaging quality or to reduce the chromatic focal shift.

4. Component characterizations

4.1 Photodiode selection

Photodiodes are photovoltaic detectors that usually have advantageous electronic and radiometric characteristics. Single element Si and InGaAs photodiodes are the best choices for the 200 nm to 1650 nm wavelength range. The photodiodes made from different materials have different energy-bands. Incident photons, with energy $h\nu$ greater than the energy band gap, will create electron-hole pairs in the semiconductor at or near the junction. Typical spectral radiant power responsivity characteristics of Si and InGaAs photodiodes are shown in Fig. 4.

These photodiodes are available in different sizes. In radiant power responsivity calibrations, the detector active area always has to be larger than the spot of the beam incident (focused) on the detector. The Hamamatsu* Model 1337 silicon photodiode is made by planar diffusion technology. The Model 2281, which is not shown here, is fabricated with the same technology. This model has a very high and spatially uniform internal quantum efficiency (does not include the reflectance loss) and it is the most frequently used photodiode in the realization and propagation of spectral responsivity functions. The Model 1227 is a PNN^+ type silicon photodiode with a thick N^+ layer that brings the $N\text{-}N^+$ boundary close to the depletion layer resulting in suppressed infrared responsivity. This model has about two orders of magnitude higher shunt resistance than the 1337. The 1227 is very suitable for photometric measurements and also for very high sensitivity applications. The extra thin P layers in both silicon models produce high ultraviolet responsivity. The photodiodes are hermetically sealed in a case. The window should not be removed to protect the photodiode against slow degradation of responsivity.

The non-uniformity of spatial responsivity of these devices has to be matched to the uncertainty requirement of a radiant power responsivity measurement. The spatial non-uniformity of responsivity (ratio maximum-to-minimum) of high quality large-area silicon photodiodes is between 0.3 % and 0.5 %, that of InGaAs photodiodes is 0.5 % or higher. Ge photodiodes have non-uniformities of about 1 % or higher. Selections of photodiodes for spatial uniformity of responsivity can be necessary if radiant power responsivity measurements are needed with reduced relative uncertainties. For broad-band applications, the spectral dependence of the spatial uniformity should be tested.

Several photodiode radiometric-characteristics to be known are temperature dependence of responsivity (if temperature control is not applied), linearity [5], and stability. The temperature dependent responsivities of the four popular photodiodes of Fig. 4 are shown in Fig. 5. At low irradiance levels, the linearity of silicon photodiodes has been verified in a extremely wide dynamic range of 11 decades, an example over 6 decades is shown in Fig. 6.

Detector electronic characteristics that can influence radiation thermometer performances are shunt resistance, parallel (junction) capacitance, and noise of the detector and the attached measuring circuit. The shunt resistance determines the voltage gain for the input noise and drift. The parallel detector capacitance has to be known to determine the gain equations of the photocurrent measuring electronic circuit [6]. For different photodiode impedances, different circuit solutions are needed to obtain the lowest measurement uncertainty and lowest noise [7]. The noise floor determines the sensitivity and dynamic range of photocurrent measurements. Photodiodes are usually linear down to the noise floor dominated by the circuit components of the current-to-voltage converter. The noise floor for Si photodiodes is in the 10^{-15} A range. Recently, thermoelectrically cooled regular-InGaAs photodiodes can be commercially purchased with shunt resistances equal to that of high quality silicon photodiodes. Since all noise components in the detector-circuit for these InGaAs photodiodes are similar to silicon photodiodes, silicon performance can be achieved using these cooled InGaAs detectors [8]. These silicon-performance InGaAs detectors can be used in radiation thermometers where high sensitivity is needed.

4.2 Preamplifier design

The preamplifier that measures the output electrical signal of the detector must be matched to the characteristics of the detector if high measurement performance is needed [94]. For high performance radiometric and photometric measurements the detectors are to be selected as well. Most frequently, photodiodes are used as high performance detectors that produce linear operation in a wide signal (radiant power) range when their short-circuit currents are measured.

The simplest version of a widely used photocurrent meter is shown in Fig. 7. The photocurrent of photodiode P (that has a shunt resistance R_S and a parallel capacitance C_J) is measured by a short-circuit current-meter. The current-to-voltage conversion in the current meter is realized by an operational amplifier OA and a feedback resistor R that has a parallel (stray) capacitance of C. This circuit diagram looks very simple. However, when low-uncertainty photocurrent measurements are needed in a wide dynamic signal range with a large signal-to-noise ratio in the output voltage V, the fundamental gains of the photocurrent meter should be known. The fundamental gains are the signal-gain, the loop-gain, and the closed-loop voltage-gain that all should be optimized for high accuracy measurements. Because of the limited space, only dc measurements will be discussed in detail in this report. The frequency dependent knowledge of the fundamental gains is important when the optical radiation is modulated [106]. Signal chopping can be applied to tune the signal frequency outside of the $1/f$ noise range of low-frequency (dc) measurements. Also, in a measurement, where the background signal component is large, such as in the infrared range, a chopped signal can be easily separated from the dc signal produced by the background radiation.

The load resistance (input resistance of the current meter) R_I for the photodiode is [11]:

$$R_I = \frac{R}{A} \tag{1}$$

where A is the open loop gain of the OA. For linear operation, the requirement for short-circuit photocurrent measurements is $R_I << R_S$. If the non-linearity requirement is lower than 0.01 %, R_I must be four orders of magnitude smaller than the shunt resistance of the detector.

For low uncertainty photocurrent measurements, the photodiodes have to be selected for shunt resistance. After selecting the photodiode, the other passive components of the feedback can be calculated. Usually, R is changed in decade increments to cover a wide dynamic signal range. Accordingly, the parallel C capacitors are to be calculated for all R selections to optimize the three fundamental gain equations for all R. Thereafter, an OA has to be selected which satisfies the noise, drift, input current, offset voltage, and speed (bandwidth) requirements. The uncertainty of the photocurrent-to-voltage conversion also depends on the photodiode selection. The current-to-voltage conversion can be described by the signal (transimpedance) gain. For low frequecy (dc) measurements:

$$A_I = \frac{V}{I_P} = R\frac{1}{1-G^{-1}} \tag{2}$$

where I_P is the output current (photocurrent) of the photodiode and G is the loop gain. The photocurrent-to-voltage conversion R, which is the signal gain, will be accurate only if $G>>1$ at the signal frequency. This is a very important design requirement for the photocurrent measuring analog control loop when low measurement uncertainty is needed from a radiometer. E.g., for a 0.02 % photocurrent-to-voltage conversion uncertainty, G should be 5000 or higher.

The loop gain for dc measurements is:

$$G = A\beta \tag{3}$$

where $\beta = R_S/(R_S+R)$ is the dc voltage attenuation of the OA feedback network.

If a photodiode with high R_S is selected, the feedback attenuation β will be close to unity, resulting in high G. The feedback resistors R of the OA can change from about 1 kΩ to 100 GΩ. A photocurrent meter (which is an analog control loop) can operate in the linear regime when these feedback resistors are used. At R=10^{12} Ω the current-to-voltage conversion becomes non-linear. Using R=10^{11} Ω, the settling time of the output voltage V can be two minutes. With the right design, R_S and R should be similar to each other and R=10 GΩ is usually enough to perform very low noise in the output voltage V of the current meter. With a maximum R=10 GΩ selection, the settling time will be less than 17 ms. The loop-gain must be high enough at the signal frequency (the chopping frequency in ac measurements) for all R selections to perform current-to-voltage conversions with low uncertainty.

The closed loop voltage gain is the reciprocal of β. It is equal to the inverse attenuation. It determines the voltage amplification for the input noise and drift. If R_S is selected high, β can be close to its maximum of unity resulting in a voltage gain not much higher than unity.
Selection of photodiodes for C_J is important for ac applications. If $AC >> C_J$, the frequency-dependent roll-off of the signal gain is determined by the integrating time constant:

$$\tau = RC \tag{4}$$

E.g., C_J of a Ge photodiode can be 36 nF as compared to the C_J =0.5 nF of an InGaAs photodiode. Because of noise amplification (boosting), Ge photodiodes are suitable only for slow dc measurements (0.1 Hz or smaller electrical bandwidth) when high signal-gain (R=1 GΩ) is needed. InGaAs photodiodes can measure 10 Hz (chopped) signal without noise boosting.

At the OA output, the signal-produced voltage V has to be always much larger than the superimposed total noise voltage originating from the noise components of the photodiode current meter. The signal-to-noise ratio at the current meter output has to satisfy the uncertainty requirement of a measurement. The signal-to-noise ratio will also depend on the noise pick up. To avoid noise pick up, the wires between the photodiode pins and the OA inputs must be short, rigid (moving free), and electrically shielded. The best results can be obtained if the photodiode and the preamplifier are combined in an electrically shielded (metal) measuring head. The power supply should be located in a separate shielded box which is connected to the measuring head with a shielded cable. The shielding to the measuring head should propagate from the electric power line outlet (using a 3-pin line connector) through the shield of the cables. In order to avoid unwanted signal pick up through ground-loops, the common (ground) lead of the preamplifier circuit should be combined with the electrical shield in one point only which should be the 0 V output pin of the power supply (typically +/- 15 V). The high resistance components in the preamplifier, including the printed circuit board (PCB) shown in Fig. 9, should be kept clean to eliminate shunt effects such as leakage currents.

The dc signal-gain (V/I_P) of a preamplifier must be known or calibrated against high accuracy standards, such as resistor standards or current-source standards. In order to avoid tedious and limited accuracy signal-gain calibrations, the feedback resistors (R) should be purchased with a 0.01 % uncertainty (tolerance) of their decade nominal values. Such resistors are commercially available from 1 kΩ to100 MΩ with a resistance temperature coefficient of 10 ppm/degree C. The R=1 GΩ signal-gain can be calibrated against the R=100 MΩ signal-gain by measuring the same constant (stable) input-current (or optical radiation when the detector is connected to the preamplifier input). In order to utilize the 0.01 % uncertainty of resistors R, a beam shutter should be used at the input of the radiometer. The output offset voltage of the preamplifier can be canceled out from the measurement by subtracting the dark reading (shutter closed) from the signal + dark reading (shutter open) at the output of the preamplifier (or the following digital voltmeter). Using this method, the temperature control can be saved in a large number of photodiode-preamplifer applications.

Care should be made at gain switching when ac signals are measured and decadic feedback resistors are used. If the signal frequency is higher than the 3 dB upper roll-off frequency, the signal-gain operating point will be on the slope of the signal-gain versus frequency curve. As the 3 dB roll-off frequencies cannot be tuned exactly to the same value at all gain selections, the actual gain changes will be different from decade even if the feedback resistor are different from each other exactly by an order of magnitude. In this case, the signal-gains are to be calibrated at the signal frequency.

Usually, integrating-type digital voltmeters measure the preamplifier output voltage for the duration of 100 power line cycles (NPLC=100) of 1.7 s to avoid long measurement (averaging) times. An rms photocurrent noise floor of 1.5 fA was measured with NPLC=100 on an optimized silicon photodiode current meter when R was selected to a maximum of 10^{10} V/A (to avoid long settling times and high resistor noise). The practical sensitivity limit in the ac measurement mode (with a 10 s integration time constant) was 0.1 fA. The conclusion from comparing the ac and the dc photocurrent measurement modes is that well-designed preamplifiers can measure weaker optical signals in ac mode with shorter measurement times.

The optimized silicon photodiode current meters can be used as building blocks of radiation thermometers. These thermometers have a signal (radiant power or photocurrent) dynamic range of greater than 14 decades.

4.3 Preamplifier gain calibration

Improved conversion uncertainty can be achieved for test current-to-voltage converters when they were calibrated against a current-to-voltage converter standard [12]. The low uncertainty gain calibrations could be extended to the 10^{10} V/A gain of test current-to-voltage converters. The 10^9 V/A gain of the converter standard was calibrated against the 10^8 V/A gain by measuring the output voltage ratio with the two gains when applying the same 5 nA constant current to the input of the converter standard.

Figure 8 shows the simplified scheme of the substitution type current-to-voltage converter calibration. The current from the variable-output stable-current source is measured with the current-to-voltage converter standard.

The current I from the electronic current source is introduced into the current-to-voltage converter standard. The output voltage V_1 is measured with a digital voltmeter. The value of the input current can be calculated after two output voltage measurements:

$$I = \frac{V_1(I) - V_1(I = 0)}{R} \tag{5}$$

where $V_1(I)$ is the converter output voltage for input current I, $V_1(I = 0)$ is the converter output voltage for $I = 0$, and R is the selected feedback resistance of the converter. The voltage subtraction cancels the output offset voltage of the converter standard.

After the determination of I, test current-to-voltage converters can be substituted for the converter standard at points A, B, C, and D. Points B and D are the “common” of the circuits that also give the electrical shielding for the connecting cables.

The output voltage of a test current-to-voltage converter is V_2. The signal-gain of the test current-to-voltage converter is:

$$G_S = \frac{V_2(I) - V_2(I=0)}{I} \tag{6}$$

where $V_2(I)$ is the test converter output voltage for input current I, $V_2(I = 0)$ is the test converter output voltage for $I = 0$, and I is the current as determined by Eq. 5. The output offset voltage of the test converter is canceled out by the voltage subtraction in Eq. 6. In order to obtain high signal-to-noise ratios, $G_S = R$ is the best choice. However, when $G_S = 10^{10}$ V/A in the test converter, the maximum built-in feedback resistance of $R = 10^9$ V/A is used in the converter standard. The uncertainty of a voltage measurement, using the HP3458A Multimeter, was 2 μV/V**.**

The circuit diagram of a traditional photocurrent-to-voltage converter is shown in Fig. 9. The smallest feedback resistor is R1 = 10^4 Ω and the largest one is R7 = 10^{10} Ω.

The loop gain of the converter standard, that determines the current-to-voltage conversion uncertainty, must be at least 10^4 V/V to obtain a conversion uncertainty of 0.01 %. This corresponds to a minimum required shunt resistance for a transfer standard (such as a trap) detector of 10 MΩ. The uncertainty obtained with the above method, at the 10 GΩ maximum feedback resistor of a test current converter was 0.013 % (*k*=2).

4.4 Spectral Filters

Radiation thermometers which operate in the visible or the near-infrared wavelength region are typically constructed using spectral filters to restrict the incident radiation on the diode to a selected wavelength region. The spectral filters can be constructed using interference layers deposited on glass substrates or constructed filter using broad-band absorbing glasses [[13]]. The interference filters are constructed using multi-layer thin film deposition, and the thin films can be much more susceptible to temperature and humidity changes than the broad-band absorbing glass filters. Since the spectral transmittance of the interference filters is critically dependent on the film thickness, any change in the film thickness due to temperature or humidity related expansion of the thin films will lead to an unwanted change in the spectral transmittance. The increasing use of "hard" or ion-assisted deposited thin films has reduced the temperature and humidity related changes[14]. For the most stable operation, the spectral filters should be temperature stabilized. If the thermal link to a heat sink is an issue, then the filters could be stabilized at slightly higher than the ambient temperatures to reduce the electrical power usage and the thermal load.

5. System level characterizations

Once the radiation thermometer is constructed from the individual components consisting of the lenses, detector and preamplifier into a system, then the system level characterizations are needed. The desired uncertainties of these system-level characterizations depend upon the temperature range and the use of the radiation thermometer. For the realization of ITS-90 below 962 °C, the spectral responsivity characterization of the radiation thermometer should be performed to determine that the spectral responsivity does not coincide with any of the atmospheric absorption lines. The atmospheric transmittances for 1 m path at sea level and 296 K temperature are shown in Fig. 10. Since the temperature calibration of the radiation thermometer will be performed using a set of fixed-point blackbodies or a variable-temperature blackbody, a low uncertainty spectral responsivity characterization is not critical. The nonlinearity characterizations are also not critical since the interpolations using the blackbody source will account for nonlinearities in the radiation thermometer. For the realization of the ITS-90 above 962 °C, the spectral responsivity measurements and the linearity characterizations are critical since both measurements will be used along with one of the Ag-, Au- or Cu-fixed point blackbodies to extend the temperature scale to higher temperatures. The size-of-source effect characterizations will still be needed in both cases since the radiation thermometer will be used with sources of different size openings.

5.1 Spectral Responsivity measurements

5.1.1 Measurement Geometry

The calibration of spectral responsivity requires the use of standard detector. Although thermopile or pyroelectric detectors could be used to derive the scale, modern radiometric realizations are performed using cryogenic, electrical-substitution radiometers. The thermopiles and pyroelectric detectors have low responsivities and resulting high noise at the typical output from a monochromator. Since the primary standard cryogenic radiometers measure radiant power, the calibration transfer starts from power mode typically using a Si-trap detector. The radiant power mode measurement geometry is illustrated for a laser beam in Figure 11. Underfilling of the detector sensitive area by the incident beam is a widely used radiant power measurement technique. Application of an aperture in front of the detector is not needed for power measurements. The uniformity of the spatial responsivity of detectors, calibrated in underfilled mode, has to be sufficiently high to keep the relative standard uncertainty low for power measurements. Measurement of stabilized laser beams is commonly applied in responsivity calibrations where the reference detector is a cryogenic radiometer or a multiple-input-reflection Si-trap detector standard.

In spectral radiant power responsivity measurements, where broadband-sources are used with either narrow-band filters or monochromators, the incident beam is usually convergent onto the detectors. These calibrated Si-trap detectors are then used in either laser-based facilities or in monochromator-based setups. Since only a few national laboratories have laser-based facilities, the more commonly used monochromator-based facility will be first described. The laser-based facility will be described later in the section on realization of thermodynamic temperatures.

5.1.2 Monochromator-based calibration setup

At most laboratories, monochromator based measurement setups are used for spectral responsivity calibrations. The best results can be obtained with the smallest complication if similar type test and working standard detectors are used which have high sensitivity in a limited wavelength range.

A typical monochromator-based responsivity measurement setup is shown in Fig. 12. A broadband lamp is imaged onto the input slit of the monochromator using lens or mirror imaging systems. Mirrors have no internal reflections, unlike lenses and are preferable for wide spectral range applications because they show no chromatic aberrations. Spherical mirrors are most commonly used for imaging, operated at near-normal angles of incidence to reduce off-axis aberrations. Spherical aberration is usually negligible for slow (i.e., F/8 or greater) mirrors.

Double monochromators are used in high accuracy applications where high stray light rejection is needed. Single monochromators have higher throughput but lower performance in terms of spectral stray light. The dispersing elements are either prisms or gratings. The dispersion of prisms is highly non-linear. Therefore, when constant spectral bandpass is needed, elaborate cams have to be used for both the wavelength and the slit-width drives. It is difficult to find prism materials that have high enough transmission and dispersion in a wide wavelength range. Prism monochromators are more complex, hence, more expensive than grating versions. Gratings have anomalies that render their spectral efficiency highly irregular and they need order sorting (cut-on) filters. The output slit is imaged at the surface of the detectors. A light shutter can be used to subtract both the output offset voltage of the detector-amplifier from the output signal.

A monochromator-based setup can be used for irradiance mode calibrations if the output beam of the monochromator is collimated and spatially uniform. For radiance responsivity calibrations in the case of radiation thermometers, an integrating sphere with a large enough exit port can be used which is irradiated by the monochromatic output beam from the monochromator. In this case, the exit port radiance of the sphere can be determined against an irradiance mode detector standard. If the signal from the integrating sphere is not sufficient, then the exit slit or the opening of the monochromator can be directly imaged by the radiation thermometer. The output from the monochromator will not be spatially or angularly uniform nor will it be truly monochromatic due to the finite opening of the exit slits.

5.2 Size-of-source effect

In many fields of radiometry, the unknown radiances from a defined, target area are determined by comparisons to reference radiance sources which can have different sizes and shapes of radiating surfaces. In photometry, such measurements determine the luminance of the target, and in radiation thermometry, the radiance temperature of the target is measured. Because the requirements for the uncertainties in the temperature determinations are so stringent, the need for correcting for the contributions of the surroundings is critical in radiation thermometry. In practice, radiation thermometers are used to assign the radiance temperatures of either tungsten-strip lamps or large-area variable-temperature blackbodies in comparison to these fixed-point blackbodies which have typically small, 3 mm to 6 mm diameter openings to increase their temperature uniformities [15]. These radiance comparisons can be between sources of different diameters and shapes and thus, it is important to characterize the systematic corrections or the size-of-source effect (SSE), which are necessary when comparing radiance sources of different sizes [16][17]. For the comparison of fixed-point blackbodies with the lowest uncertainties, the systematic corrections for the SSE can be one of the dominant terms in the total uncertainty budget [18].

Although SSE has been extensively studied with application to radiation thermometry [19], the effort to reduce out-of-field scatter has a much longer history in the development of coronagraphs [20]. The problem of measuring the corona, or the electromagnetic activity of the sun, is similar to the problem in the rejection of stray radiation from blackbody sources in that the intense radiation from the solar disk must be rejected in order to study the corona. A coronagraph, or a telescope dedicated to the imaging of the corona, must create an artificial eclipse within the telescope, and imaging the sun onto an opaque target performs the rejection of the direct solar radiation. The placement of the aperture stop behind the field stop is attributed to Lyot in the development of the coronagraph [21]. Furthermore, the characterization of the radiation thermometer to reduce the SSE when viewing sources with different source sizes is analogous to the characterizations required to assess the radiometric rejection properties of the coronagraph.

In radiation thermometry, the SSE has been measured using a uniform variable-diameter radiance source with a central obscuration (“indirect method”) [22] or without the central obscuration (“direct method”). Comparison studies have also been performed using blackbody cavities and radiance sources to study the effect of volume radiation of the blackbody on the SSE [23]. All three methods have been shown to be equivalent [24]. **FIX REFERENCE NUMBERS FROM HERE!!!** These studies have shown that SSE measured with a source diameter of 50 mm can be reduced to < $1x10^{-2}$ in industrial radiation thermometers and to < $1x10^{-3}$ in reference radiation thermometers. Even with large SSE, systematic corrections can be made, but these corrections require knowledge of the spatial distribution of the source radiance, and the spatial uniformity can also be dependent on time-varying environmental conditions. The reduction of the SSE to < $5x10^{-5}$ would eliminate the need for measurement of the spatial uniformity, and the SSE could be considered as one of the uncertainty components in the total uncertainty budget.

5.2.1 Measurements of SSE

The studies of the SSE could be performed using a light-tight optical bench such as shown in Fig. 13. The light-tight box around the base plate is constructed of anodized, extruded aluminum. The walls of the light-tight box are formed of opaque-black plastic and covered with an internal black appliqué, Ultrapol. A circular opening of 64 mm diameter with a sharp, beveled edge is machined on the front plate to act as the front baffle, and the objective lenses are placed on a 6 cm long V-groove mount placed behind this opening. The V-groove optical mount is designed for quick interchange of objective lenses for testing purposes. An adjustable iris with a sharp, well-defined inner edge is placed between the front baffle and the objective lens and is used to reduce the aperture to 44 mm diameter so that the ground-glass edge of the objective lens is not illuminated. The side of the iris facing into the radiometer is also covered with the black appliqué, to reduce the back reflectance onto the objective lens.

The 1 mm and 0.6 mm diameter field stops are fabricated from a bimetal BeCu/Ni substrate with black anti-reflective coated and metal-reflective sides. The field stop is tilted about 10° from the optical axis to avoid back reflections toward the objective lens. The direct reflection from the field stop is directed toward the front corner of the radiometer, and since the entire inside of the radiometer is covered with low-reflective black covering, the direct reflectance from the field stop is suppressed. The metallic side of the field stop was placed toward the object side for use in possible alignments with laser illumination and to visually align sources. The field stop, the aperture stop, the collimating lens and the detector are all placed on movable holders on an optical bench so that the physical configuration could be quickly changed. A variable-aperture iris could also be placed between the field-stop and the detector to act as a limiting aperture stop or a Lyot stop.

A quasi-monochromatic radiance source of 50 mm diameter is used as the source [25] as shown in Fig. 14(a). **THIS FIG IS MISSING!** The LED source utilizes 36 LEDs placed on a 50 mm diameter circuit board and can be temperature stabilized using a thermoelectric cooler. Since the LED source is nearly monochromatic and the spectral radiance is centered at 660 nm, spectral filters are not used. The spectral radiance of the LED source shown in Fig. 14(b) **THIS FIG IS MISSING!** was measured using a spectroradiometer by reference to a NIST-calibrated tungsten-strip lamp. The spatial uniformity of the LED source is measured to be varying by ± 2 % over the central 40 mm region with the edge radiance falling to about 60 % of the central radiance. The temporal stability of the LED source was monitored using a photodiode attached to the side of the LED source. The low-reflectance central obscuration was constructed with a hard polymer shaped into a conical-cavity shape to reduce the back-reflectance [26]. The 2 mm central obscuration was glued into place in the centered hole in the front ground-glass diffuser plate. The diameter of the LED source was changed using a variable-aperture steel iris, which could be adjusted from 2 mm to 50 mm diameter. The physical separation of the iris to the front diffuser was minimized to reduce the back reflections from the rear of the iris into the central obscuration.

Although an LED source was used for these measurements, typically, integrating sphere sources are used with a central obscuration. The central obscurations are constructed using opaque materials formed into a small blackbody to reduce the reflectance. The central obscurations are made with larger diameters than the target size to avoid scattering from the edges of the obscuration. Due to the limited sizes of integrating spheres, it is difficult to measure large > 30 cm diameter SSE.

Alternatively, if the radiation thermometer is stable, a small integrating sphere or another lambertian source could be translated in the x and y planes to simulate a much larger diameter source. Studies have shown the equivalence between the direct, the indirect and the translation methods.

5.2.2 SSE Determination

The SSE contribution of different objective lenses and changing optical designs were tested by plotting the ratios of signals,

$$\sigma(d, d_o) = \frac{\mathrm{v}(L, d) - \mathrm{v}(L, d_o)}{\mathrm{v}(L)}, \tag{7}$$

where d is the diameter of the uniform radiance source, d_o is the diameter of the central obscuration, and L is the radiance of the source. The signal measured while viewing the unobstructed radiance source is v(L), the signal measured while viewing the central obscuration with the diameter of the radiance source, d, is v(L,d), and the signal measured with the diameter of the variable aperture at the diameter of the central obscuration, d_o, is v(L,d_o). If stray radiation during the measurements is suppressed then the signal v(L,d_o) should be equal to the signal with the radiance source turned off. Optimally, the signal from monitor diode attached to the side of the source should be used to determine if the radiance of the source changed for any reason during the measurements. The output from integrating sphere sources could depend on the size of the opening.

5.2.3 Importance of the Lyot stop

The SSE measurements shown in Fig. 15 are performed with the Lyot stop (or glare stop). The placement of the Lyot stop is determined by the focal length of the objective lens and the collimating lens in Fig. 12. The purpose of the Lyot stop is twofold. The Lyot stop is used to block radiation originating from internal scatter away from the objective lens, and the Lyot stop also is used to block the diffracted radiation from the edge of the objective lens. The Lyot stop then becomes the limiting aperture stop in the radiation thermometer and should be placed at the image distance of the collimating lens with the distance from the collimating lens to the objective as the object distance,

$$\frac{1}{\mathrm{i(o)}+\mathrm{f(c)}}+\frac{1}{\mathrm{i(c)}}=\frac{1}{\mathrm{f(c)}}, \tag{8}$$

where i(o) is the image distance of the objective lens or the distance from the objective lens to the field stop, f(c) is the focal length of the collimating lens, and i(c) the image distance or the Lyot stop distance from the collimating lens. Placement of the aperture stop at any other position after the collimating lens would not be effective in blocking the diffracted radiation from the objective lens and would not be considered a Lyot stop. Furthermore, if multiple-element objective lenses are used, then there would have be a corresponding increase in the number of stops since the scattering from the individual surfaces in the objective lens system would appear as volume scatterers.

The importance of using a Lyot stop is shown in Fig. 16. The SSE was measured using the same 250 mm focal length (fl) achromat lens with the Lyot stop and also without the collimating lens and the Lyot stop. For measurements without the Lyot stop, the Si diode was placed directly behind the field stop. The SSE increases rapidly as the diameter of the source is increased resulting in a factor of 20 increase in the SSE at 50 mm as compared to the measurements with the Lyot stop.

The diameter of the Lyot stop depends on the focal lengths of the objective lens and the collimating lens since the de-magnification factor, M, is

$$M=\frac{\mathrm{i(o)}+\mathrm{f(c)}}{\mathrm{i(c)}}. \tag{9}$$

Thus for a 200 mm focal length objective lens in Table 1 with a 50 mm focal length collimating lens, the de-magnification factor, M, is 6.66. We found that a 6 mm diameter Lyot stop was effective in reducing the SSE, which corresponds to a 6 mm x 6.66 ≅ 40 mm diameter aperture stop at the plane of the lens leading to a reduction of the objective lens diameter by about 4 mm. Further reductions in the Lyot stop diameter will lead to lower SSE but at the expense of decreasing the throughput of the radiometer.

5.2.3 Understanding the source of the SSE

An analogy of the indirect method of measuring SSE and dark-field imaging in microscopy can be made to understand the contribution of scatter from the objective lens. In dark-field imaging as illustrated in Fig. 17a, the annular stop leads to illumination of the sample at oblique angles. The direct illumination is not collected by the microscope objective, and only the scattered light from the sample is collected by the microscope objective. In the SSE measurements as shown in Fig. 17b, the annular stop is replaced by the radiance source with a central obscuration, and the sample is replaced by the objective lens of the radiation thermometer. If there were perfect imaging with no scattering, then no radiation would be collected by the objective just as no radiation would be scattered into the field stop of the radiation thermometer. If the scattering within the radiation thermometer is reduced, then any radiation through the field stop is primarily from the scattering from the objective lens.

Any defects or particulate contamination on the objective lens acts as a secondary source at the plane of the objective lens. Increasing the diameter of the SSE test source increases the radiation incident on the defects on the objective lens or the irradiance (W / cm^2). The increase in the irradiance on any particles leads to a corresponding increase in the radiance of the particle resulting in an increase in the SSE. Thus it is critical to reduce the irradiance on the objective lens by the use of front baffles and the use of low-reflectance inner walls on the radiometer. Since the defects on the objective lens act to collect radiation, it is important to shield the objective lens from stray radiation as much as possible.

Since any surface contamination can lead to an increase the scatter, prior to the SSE measurements, all lenses were cleaned using the following procedure. The lenses were cleaned for dust using compressed air and then wiped clean with an ethyl-alcohol-moistened lens tissue. To remove the cleaning marks from the wiping process, the lenses were then cleaned using a single-sheet drag technique with a single drop of ethyl alcohol. The solvent for lens cleaning should have a high evaporation rate so that residues are not left on the lens. The lenses were again sprayed with the compressed air to remove any lens-tissue particles. Such cleaning of the lenses was possible since the lenses could be removed from the mounts and handled by their edges. The SSE was found to be critically dependent on the cleanliness of the lens with an increase in the SSE by about 10 % or more with few dust particles on the surfaces of the objective lens. Since cleaning residues will also scatter radiation, any cleaning marks also lead to an increase in the SSE.

The scattering from large particulate contamination of the objective lens and from defects on the objective lens is difficult to describe and may depend upon the size, the shape and the material of the scatterer. Small particles scatter primarily in the forward direction as described by Rayleigh scattering [[27]], and since the scattering has a $1/\lambda^4$ wavelength dependence, one would expect that reducing the SSE would be more difficult at the shorter wavelengths as well. If the scattering is more isotropic than forward-directed, then the use of a long image distance could be beneficial in reducing the contribution of objective lens scatter.

Due to the contribution of scatter from the objective lens in increasing the SSE, any windows placed between the objective lens and the blackbody will also lead to an increase in the SSE. The imperfections and the particulate contaminations on the window surfaces will act to scatter radiation into the field stop. Thus if any changes are made to the optical path from the source to the radiation thermometer, the SSE should be measured prior to the use of the modified radiation thermometer.

The placement of the aperture stop is also important in reducing the SSE. If the aperture stop is placed at the front of the objective lens, then the diffracted radiation from the edge of the aperture stop cannot be removed. Just as the radiance of the objective lens defects increases as the incident irradiance is increased from the larger diameter of the SSE source, the amount of diffracted radiation will increase from the greater irradiance incident at the edge of the aperture stop. If the limiting aperture is placed in front of the objective lens, then the SSE is expected to increase as the aperture stop diameter is decreased since the diffracted edge is pulled in closer to the center. However, if a Lyot stop is used, then the SSE should decrease as the Lyot-stop diameter is decreased since more of the diffraction from the edge of the objective lens is removed. Thus the placement of the aperture stop is important in understanding the dependence of the SSE on the aperture stop diameter.

5.2.4 Importance of optical performance

Poor imaging performance of the objective lens can also lead to an increase in the SSE. The main considerations for optical performance can be divided into chromatic aberrations and other optical aberrations such as spherical aberrations, coma, and astigmatism, among others. The chromatic aberrations are considered separately since the radiometer can be refocused to minimize chromatic aberrations while the other types of optical aberrations require a redesign of the lens. Most commercial achromatic doublets are optimized for infinite conjugate and can provide diffraction-limited performance under infinite conjugate operation. These lenses are not diffraction limited with 1:1 or 2:1 finite-conjugate ratios, but custom, achromatic lens designs can be optimized for diffraction-limited performance at 1:1 conjugate ratios or any other conjugate ratios.

The calculated optical performances of the lens combinations evaluated for SSE in Fig. 15 are shown in Table 2. Due to the limitations of the modeling program, the GRIN lens was not evaluated. The imaging performance is evaluated using Optical Software for Layout and Optimization (OSLO) from Lambda Research although any other optical modeling program can be used. The calculations are performed at 650 nm with a 1 mm diameter object size and 44 mm diameter aperture top at the entrance of the objective lens system. The imaging at the focus plane of the field stop is quantified by comparing the diffraction-limited radius with the geometric-root-mean-squared (RMS) radius and by the Strehl ratio. If the ratio of the diffraction-limited radius and the geometric-RMS radius is < 1 then the system can be considered to be diffraction-limited with other sources of optical aberrations well controlled. The Strehl ratio is a measure of the point-spread function and is equal to 1.00 for a perfect imaging system.

In Table 2, the optical imaging quality of the doubled achromat objectives is evident from the near unity Strehl ratio and the diffraction-limited performance. Doubled achromats with matching focal lengths or with mismatched focal lengths are known for diffraction-limited imaging performance, however, due to the inter-reflections between the lenses the SSE is increased by about x 4 greater than the single lens as evidenced in Fig. 15. The measurements in Fig. 15 for the double achromats were performed with the same lenses used for the single achromat measurements so that the SSE should be not subject to the differences in the quality of the lens surfaces. Although the optical performances of the single achromats used at finite conjugate is far from diffraction limited, the SSE found to be lowest with the single achromats.

At longer wavelengths, the optical performance of the single achromats improves. Table 3 shows the optical modeling of the PAC088 lens at selected wavelengths where radiation thermometers can be constructed. The imaging performance as given by the Strehl ratio increases from 0.112 at 650 nm to 0.310 at 2250 nm demonstrating that radiometers designed in the visible wavelengths can be used also in near infrared wavelength region with improved performance. There will be other considerations in the near infrared such as the anti-reflective coating on the lens and the lens transmittance.

If a single achromat with diffraction-limited optical performance is desired, then custom lenses can be designed. In Table 4, an example of an optimized lens design is given found using OSLO. Although many different glass types can be chosen for the optimization of optical performance, the most common achromat Schott glass combinations are chosen for this example. The optical performance of the optimized achromat is listed in Table 5 showing the nearly diffraction-limited performance at the wavelengths of interest. With such lenses, if the surface scatter is controlled then low SSE with good imaging is possible. Furthermore, with the choice of flint-glass and crown-glass elements in the achromat, the objective lens can be made to have small chromatic focal shifts at 650 nm and 900 nm avoiding the need to refocus at the two wavelengths.

Even with the best optical designs, the fabrication of objective lenses for the lowest scatter could be difficult since many different vendors with varying fabrication capabilities exist. For instance, we found that a contribution to SSE can arise from the scattering from the glue between the elements of the achromat. Although the surface finish of the lens can be specified by a scratch-and-dig criterion, the glue scatter cannot be specified using the surface finish criterion and would be dependent on the control of the manufacturing process. Different objective lenses with 200 mm focal length from different manufacturers were measured for SSE in Fig. 7. **WHERE IS THIS FIGURE???** For these measurements, all elements in the radiometer setup were the same except for the replacement of the objective lens. The increased scatter from the surface and interface imperfections from Thorlabs lens could be visually observed with a bright light source, and the Newport lens, PAC087, was visually observed to have lower scatter. The higher scattering is immediately observed with a greater SSE found using the Thorlabs lens.

If the radiation thermometer is to be used for only radiance ratios of blackbody sources then optical performance is not so critical. Since there is very little spatial non-uniformity in the cavities of fixed-point blackbodies or standards-quality blackbodies, achieving diffraction-limited performance can be sacrificed for low-scatter criterion. Lens-based optical systems will perform optimally for on-axis designs with worse optical performance as the imaging goes off-axis. Since radiation thermometers are designed for on-axis performance with small < 3 mm diameter target areas, the optical aberrations are minimized. If sources with greatly different spatial extents will be compared, then an assessment of the optical performance of the point-spread function or the Strehl ratio should be determined.

5.2.5 Impact of SSE

The sources of SSE in radiation thermometer are due to the internal radiometer design as well as the scatter properties of the objective lens system. If the inside of the radiometer is not coated with low-reflective material then secondary sources could be present from the internal reflections, which can be reflected back into the objective lens. To control the reflections within the radiometer, the internal dimensions should be such so that multiple reflections can be controlled and reduced.

A comparison of the SSE performance of the NIST optimized radiation thermometer with that of the Institute for Nuclear Technology and Energy Systems (IKE) Linear Pyrometer 3 (LP3) is shown in Fig. 8 [[28]] **WHERE IS THIS FIGURE ???**. The LP3 is widely used at different national measurement institutes as a standard radiation thermometer for the realization of ITS-90. The data is obtained from reference 16.

The sensitivity of the radiometers to SSE can be converted to temperature using the derivative of the Wien approximation,

$$\frac{\Delta L}{L} = \frac{c_2}{\lambda} \frac{\Delta T}{T^2} \tag{10}$$

where L is the spectral radiance, T is the temperature, c_2 is the second radiation constant and λ is the center wavelength of the radiation thermometer. The Wien approximation is valid since measurements with the Si-diode based radiation thermometers are all performed at a shorter wavelength region from the peak of the Planck radiance for temperatures ≤ 3000 K. The corrections for SSE are converted to temperatures in Table 6 using Eq. 10. The comparison shows that the NIST SSE optimized radiation thermometer is less sensitive to the SSE, and the systematic corrections, which were necessary with the LP3, could be treated as uncertainties in temperature with the NIST radiation thermometer. From the use of Eq. 10, these measurements demonstrating SSE of 3×10^{-5} with a 25 mm diameter source indicate that SSE effects of < 2 mK at 1337 K and < 9 mK at 3000 K with a radiation thermometer centered at 650 nm can be achieved.

5.3 Characterization of Linearity

5.3.1 Importance of Linearity

In radiometry or pyrometry, radiometers are often used to assign the spectral radiance or radiance temperatures of sources using ratios of signals which can differ by five decades or more. For performing ratios between such sources with low uncertainties, the linearity of the detectors used in the transfer radiometers needs to be characterized. The linearity characterizations are not so important if the radiation thermometer will be used in a temperature range where interpolations are possible. The linearity characterization becomes especially critical in the temperature range above 962 °C where the high temperatures are determined using extrapolations from lower temperatures or signals.

5.3.2 Physical sources of linearity

The linearity of photodiodes with respect to continuous radiation is mainly influenced by two effects: First, on the local minority carrier distribution within the semiconducting material and second on the current path through the device. The first effect depends on the penetration depth of the optical radiation and may result in a wavelength dependent non-linearity, if deep electron or hole traps within the semiconductor material affect the minority carrier diffusion length (particularly in lower grade silicon detectors). Second, as a photodiode is never an ideal diode, also ohmic resistances along the current path take place. Especially, at high irradiance levels, the path and terminal resistance connected in series to the junction of the diode determines the photocurrent (i.e. short-circuit output current).

5.3.3 Measurement of Linearity

There are essentially three recognized methods for assessing the linearity of optical and infrared detectors [^{29}21]: the superposition method [^{30}6, ^{31}7], the attenuation method [^{32}22], and the differential or ac method [^{33}23]. Both the superposition method and the differential method exploit the linearity test (Equation (6)), but the superposition method, first proposed by Coslovi and Righini [^{34}6], most clearly exploits the same principles as the combinatorial approach. As currently implemented, however, these methods are used only for assessing the non-linearity of optical detectors. The linear scale factors are typically determined in separate comparisons with standard sources.

The superposition method is most commonly used in the form known as flux-doubling [^{35}25]. If the linearity test is carried out with two test artefacts with attributes of the same magnitude then (6) can be rewritten as:

$$2A(X) - A(2X) = 2\xi(a) - \xi(2a)\ . \tag{11}$$

This shows that the instrument error at 2*a* can be found in terms of the two measurements and the non-linearity at *a*. Equation (11) is applied recursively so that the non-linearity is determined at 2*a*, 4*a*, 8*a*, and so on, with each expressed in terms of the sequence of measurements and the non-linearity at *a*, the lowest measurement. Thus, the non-linearity is determined at a sequence of exponentially spaced points, except for one piece of information. It turns out that the error in the first point is required only for absolute radiometry [^{36}26]. Thus the flux-doubling method enables measurement of non-linearity and an additional calibration point is required to anchor the detector response absolutely, much as described in Sections 2.2 and 2.3

Unfortunately, the flux-doubling method produces sparse, exponentially-spaced data with cumulating uncertainties. It also, unlike over-determined systems, has no surplus of data for demonstrating the validity of the non-linearity model or for estimating uncertainties.

Yoon *et al* [^{37}28], demonstrate a version of the superposition method that sums light over two paths, as with the flux doubling method, but with three filter wheels inserted into the system, as shown in Figure 18. Filter wheels one and two each have 5 positions controlled by an index *i* and *j*, respectively, with $i = 0$ and $j = 0$ corresponding to an opaque shuttered position. Filter wheel three has 6 positions controlled by index *k*, with $k = 0$ being a shuttered position. The total flux through the two paths is additive so that,

$$a_{calc}(i,j,k) = \phi_1(i,k) + \phi_2(j,k) \quad (12)$$

For a single path there are 30 possible filter combinations, of which 10 are nominally shuttered. Thus there are a total of 20 non-zero combinations of filters, or 20 different flux levels, for each path. The shuttered positions are used to compensate for the dark current of the detector, so are not included amongst the valid combinations. With all possible combinations of *i*, *j*, and *k*, there are 120 non-zero flux levels. The system is a realization of the combinatorial method with 120 measurements and 40 unknown parameters.

A least-squares fit is used to fit the 40 artifact parameters and simultaneously determine the distribution of the non-linearities. For the best solid-state detectors, no correction equation is necessary so the least-squares cost function is

$$s^2 = \frac{1}{80}\sum_i\sum_j\sum_k\left(a_{\mathrm{meas}}(i,j,k) - a_{\mathrm{calc}}(i,j,k)\right)^2 . \quad (13)$$

Standard uncertainties of 0.02 % have been achieved for silicon detectors (Figure 4), and 0.04% for InGaAs detectors.

6. Radiation Thermometry below the Ag point

Accurate determinations of radiance temperatures from 150 °C to 1000 °C are important for the calibration of radiation thermometers which are used in turn for process control or to transfer the calibration to other radiation thermometers. In this temperature range, one can establish a scale on radiation thermometers from the International Temperature Scale of 1990 (ITS-90) either by using the ITS-90 fixed-point blackbodies (FPBBs) from the In-point to the Ag-point with an interpolation equation or by using a variable-temperature blackbody (VTBB) whose temperatures are determined by contact platinum resistance thermometers (PRT) [38]. In both approaches, the FPBB or the VTBB emissivity has to be measured or modeled so that the lowest uncertainties in the transfer to the radiation thermometer can be achieved. International comparisons of scales in this temperature range have revealed that the lowest uncertainties in radiance temperatures can be achieved using the fixed-point interpolation technique instead of using a variable-temperature blackbody [39]. Uncertainties from the use of FPBBs are possibly lower since the temperatures are well known and high spatial temperature uniformity of the cavity results in a high-emissivity blackbody. Variable-temperature blackbodies are expected to have larger uncertainties arising from difficulties in achieving uniform temperature distributions within the cavity and differences in temperature between the contact thermometer and that of the radiating surface of the blackbody, thus resulting in larger uncertainties in the emissivity of the blackbody.

Although the method of calibrations using fixed-points is well established, commercial radiation thermometers which are temporally stable and able to view the small cavity openings of the FPBBs are not readily available. Furthermore, custom InGaAs radiation thermometers constructed by the national measurement institutes have conflicting designs [40,41]. Although reduction of size-of-source effect (SSE) is a critical design feature due to the need to compare small-area fixed point blackbody cavities to large variable-temperature blackbody openings, implementation of the Lyot stop has been lacking. Furthermore, in the past, methods to decrease the noise-equivalent current of the radiation thermometer have not been extensively explored.

A generalized design for an InGaAs-based radiation thermometer (RT) capable of measurements from the In-point to the Ag-point is described. The radiation thermometer also incorporates a Lyot stop while utilizing a low-scatter objective lens. The construction utilizes carbon-epoxy rods for structural stability with temporal stability of the responsivity increased by the use of a room temperature-stabilized filter and cooled detector. The detector is contained in a hermetically sealed package to decrease the detector temperature below ambient temperatures in order to increase the shunt resistance for low-noise operations.

2. RADIATION THERMOMETER CHARACTERIZATION

2.1 Physical Design

The schematic of the radiation thermometer is shown in Fig. 19. The internal elements are mounted on four 15 mm diameter graphite-epoxy rods for structural stability. The graphite-epoxy rods have a coefficient of thermal expansion (CTE) of -0.5×10^{-6} K^{-1} which is smaller than that of fused silica [42]. The rods are attached to the front plate holding the objective lens and the various separations between the optical elements can be smoothly adjusted by sliding along the through rods. The angled field stop is constructed from polished stainless steel with a beveled 3 mm diameter hole. The field stop is angled to reduce the back reflection of the image onto the objective lens, thus reducing the SSE. The specular reflection from the field stop is directed to a flat mirror for viewing through the telescope objective. The radiation through the field stop is collimated by the 70 mm focal length achromat and the plane of the objective lens is focussed onto the Lyot stop. The presence of the Lyot stop is critical in reducing the SSE. The room-temperature stabilized interference filter is constructed using hard, ion-assisted deposited layers at a center wavelength of 1550 nm. The full-width at half-maximum bandpass of the filter is 100 nm. Due to the 4-stage thermoelectric (TE) cooler which limits the maximum size of the regular InGaAs detector, a 3 mm diameter detector is used. The detector lens focusses the 3 mm diameter object at the field stop onto a 1.5 mm diameter region on the detector, leading to an underfilled detector.

The outer case of the radiation thermometer is floating with respect to the optical elements attached to the graphite rods and is only fixed at the middle supporting plate. The case is constructed using 1.83 mm thick anodized aluminum tubing. The use of the Al tube facilitates rapid thermal equilibration between the laboratory temperature and the internal temperatures. Additionally, the heat-sink plate for the InGaAs detector is thermally connected to the external tubing with copper-braided contacts which work to dissipate the heat generated from the use of the TE cooler. We are able to achieve -70 °C with only passive cooling. Additional information on the construction of the radiation thermometer is given in Table 1.

2.2 Detector optimization

The most important aspect of the radiation thermometer design is the selection of the detector to be used in the radiation thermometer. Due to the linearity and the wavelength region of the spectral power responsivity, a regular InGaAs diode was chosen. Since the small target diameter and the f/# limits the throughput of the RT, the preamplifier should have a dynamic range from 10^{10} V/A to 10^{5} V/A for measurements of blackbodies from the In-point to the Ag-point. In a transimpedance amplifier circuit, the shunt resistance of the input diode should have a value greater or equal to the feedback resistance for linear, low-noise amplification of the current. The measurement of the shunt resistances of both 1 mm diameter and 3 mm diameter InGaAs diodes in Fig. 20 shows that the shunt resistances have a semi-logarithmic relationship to temperature. The shunt resistances also increase as a linear function of the detector area, as expected for defects with a uniform surface density. Fig. 20 shows that for 1 mm diameter diodes, shunt resistances > 10^{10} Ω are achieved at detector temperatures of - 20 °C, which is possible with 2-stage TE cooling. For 3 mm diameter diodes, detector temperatures of at least - 40 °C are needed to achieve > 10^{10} Ω shunt resistance. Unless the diode material quality is improved, larger diodes are expected to require greater cooling to obtain the same shunt resistances.

2.3 Temperature-dependent detector performance

The importance of the ability to cool the detector to below ambient temperature is shown in Fig. 21. The equivalent dark current and the standard deviation of it at a preamplifier gain of 10^{10} V/A are shown. The standard deviations are calculated from 10 measurements made during the period of 10 power-line cycles (NPLC) that corresponds to an electrical bandwidth of 0.13 Hz. The equivalent dark current, calculated from the output offset voltage and the current-to-voltage conversion, is only weakly dependent on the detector temperature with a decrease from 3 pA to about 1 pA as the detector is cooled from room temperature to -70 °C. The change in the equivalent dark current with decreasing temperature indicates that stabilizing the detector temperature is important in avoiding drift in the output signal, especially at the In point where the net photocurrent is only about 23 pA. With cooling of the detector, the standard deviation of the dark current (the noise equivalent current) changes much more, from about 100 fA to 2.4 fA. Although the detector was cooled to lower temperatures than -70 °C, the heat generated from the

TE coolers could not be readily dissipated which lead to self heating of the detector. We observed a slow drift of the equivalent dark current when the temperature of the detector was set to lower temperatures that precluded stable measurements of the noise equivalent dark current. These measurements indicate that close to Si-type performance of a few fA noise-equivalent current [43] is possible with 4-stage TE cooling. This low-noise performance is especially important at the In-point where any decrease in the noise-equivalent power directly leads to a decrease in the noise-equivalent temperatures.

2.4 Optical Performance

The InGaAs radiation thermometer utilizes a commercial 50 mm diameter achromat with a focal length of 200 mm with nearly 1:1 finite-conjugate imaging. Since commercial achromatic lenses are designed for infinite-conjugate imaging, the imaging performance suffers as shown by the Strehl ratio in Table 4. The Strehl ratio increases as the wavelength increases which indicates that imaging performance is better at 1550 nm than at 500 nm. Furthermore, achromatic lenses will generally have two wavelengths where the image distances will be equal for a set object distance with the chromatic focal shift depending on the lens material and thickness. Since the radiation thermometer is designed to transfer a temperature scale from one blackbody to another without any desired spatial structure within the cavity, the need for imaging performance is much reduced. Table 3 shows that although the alignment of the radiation thermometer can be performed in the visible wavelength, the object distances at 1550 nm and at 500 nm differ by 25 mm for the same image distance. Since the internal focus is difficult to adjust, the object distance can be offset by this difference to account for chromatic aberrations.

3. Blackbody measurements and interpolation functions

The InGaAs radiation thermometer was calibrated using the ITS-90 fixed-point blackbodies at the freezing temperatures of In, Sn, Zn, Al and Ag. The freezing-point cavities have internal openings of 6 mm diameter which is larger than the 4.5 mm spot size of the NIRT1, and thus the opening overfills the radiation thermometer. The freezing-point cavities are inserted into furnaces with heat-pipe liners to ensure the spatial uniformity during the melts and freezes. The freeze duration lasts for about 30 minutes, and these measured net currents shown in Table 6 are the results of averaging many samples. The measured photocurrent, *i*, at the 5 fixed points are fitted using a modified-Planck function[44],

$$i = \frac{\mathrm{A}}{\exp\left(\dfrac{\mathrm{c}_2}{\mathrm{B} * T + \mathrm{C}}\right) - 1}, \tag{14}$$

where T is the temperature in kelvin, c_2 is the second radiation constant, and A, B and C are the fitting parameters. The nonlinear minimization to determine the fitting parameters can be performed using Excel or another fitting program. The fitted parameters are shown in Fig. 22 along with the photocurrents which were measured at the respective temperatures.

The residuals of the fit shown in Table 6 can indicate whether the measurements at any fixed point are in agreement with the overall fitted curve. The residuals shown as percent differences from the fitted curve indicates that the Sn-point measurements are off from the rest of the freezing-points which have much smaller residuals.

A major advantage of the modified-Planck function is that the function can be inverted to

$$T = \frac{1}{\mathrm{B}}\left(\frac{\mathrm{c}_2}{\ln\left(\dfrac{\mathrm{A}}{i} + 1\right)} - \mathrm{C}\right), \tag{15}$$

which gives the relationship between the measured photocurrent and the temperature.

4. Uncertainties

The uncertainties of the NIRT1 can be broadly classified into those related to the fixed-point blackbodies, characterizations of the radiation thermometer and the use of the radiation thermometer. In Table 1, the standard uncertainties are listed as either temperature uncertainties or percent uncertainties. The values are either from Ref. 10 **???** or obtained from the NIRT1 characterizations. The standard uncertainties in Table 7 are converted to temperature uncertainties using the Eq. 2 **???** **(Eq numbers are to be fixed!)** to obtain the temperature uncertainties in Table 8.

3. Possibility of thermodynamic temperature determinations below Ag-freezing temperature

Thus far, radiation thermometers with InGaAs detectors have only been used to transfer the source-based ITS-90 scale to other sources or blackbodies. Due to the developments of laser-based calibration facilities and the low-noise and high linearities of InGaAs detectors, the possibility of detector-based thermodynamic temperature determinations are being explored. The detector-based calibration of the InGaAs radiation thermometer would be performed in a similar manner as for a Si-diode based radiation thermometer [45], but instead of using a Si-trap detector, a spatially uniform InGaAs detector would be used in place of the Si-trap detector. A possible replacement for the Si-trap detector in the near-infrared wavelength region has been constructed using an integrating-sphere receiver and four, InGaAs detectors[46]. A transfer radiometer would need to be calibrated for spectral power responsivity by comparison to the cryogenic, electrical–substitution radiometer using infrared lasers, and thus the optical power scale would be derived from the electrical power. The transfer radiometer would need a precision aperture and known spatial uniformity of responsivity so that the power responsivity can be converted to spectral irradiance responsivity. The conversion to irradiance responsivity can be performed with detectors in a trap configuration or with detectors that are attached to integrating sphere inputs. With a laser-irradiated sphere along with the calibrated transfer radiometer, the InGaAs radiation thermometer can be calibrated for absolute detector-based radiance responsivity. Since Spectralon* and other sintered or packed polytetrafluoroethylene (PTFE) materials have a high reflectance at 1.55 µm, integrating spheres have high throughput and spatial uniformity. It is anticipated that such a detector-based radiation thermometer could be calibrated to 0.05 % (k = 2) [47]. The resulting thermodynamic temperature uncertainties are shown in Table 5.

4. Calibrations of radiation thermometers using the International Temperature Scale of 1990 (ITS-90)

The temperatures above the freezing temperature of Ag are determined using Planck radiance ratios to the Ag, Au or Cu fixed-point blackbodies[48]. The extrapolations to higher temperatures from the fixed point are performed from the relative spectral responsivity, *S(λ)*. The radiance ratios are determined using integrated Planck radiances, *L*, convolved with the spectral responsivity[49],

$$\frac{L(\lambda_m, T_1)}{L(\lambda_m, T_0)} = \frac{\int S(\lambda) \cdot L(\lambda, T_1)}{\int S(\lambda) \cdot L(\lambda, T_0)}, \qquad (16)$$

where λ_m is the mean effective wavelength. Since the Planck radiances changes as a function of temperature and materials can have spectrally dependent emissivities, the spectral responsivities are reduced to an effective wavelength[50], λ_e, with

$$\frac{1}{\lambda_e} = \frac{\int \frac{1}{\lambda} S(\lambda) \cdot L(\lambda, T)}{\int S(\lambda) \cdot L(\lambda, T)}. \tag{17}$$

The concept of an effective wavelength enables the use of Planck radiances at a single wavelength to replace the spectral responsivity of the radiation thermometer with a delta function spectral width although the radiation thermometer has a finite spectral width. Since the radiance ratios in Eq. 16 are performed at different temperatures, the radiance ratio is determined at a mean effective wavelength,

$$\frac{1}{\lambda_m} = \frac{1}{2} \cdot \left(\frac{1}{\lambda_m(T_0)} + \frac{1}{\lambda_m(T_1)} \right). \tag{18}$$

In practice, the measured photocurrents at the two temperatures are compared using

$$\frac{i_1}{i_0} = \frac{L(\lambda_m, T_1)}{L(\lambda_m, T_0)}, \tag{19}$$

And the unknown temperature, T_1, is obtained from the ratios of Planck radiances at the mean effective wavelength which matches the measured photocurrent ratios. With the widespread use of computers, the usage of effective wavelength is reduced since the integrals can be easily evaluated using spreadsheet programs.

Alternatively, since the wavelength integrals can be easily evaluated, the implementation of ITS-90 can be performed without the use of the mean effective wavelength concept. Since only the relative spectral responsivity is obtained from the typical monochromator-based calibrations described above, the absolute throughput of the radiation thermometer, τ_{abs} needs to be determined from the measurements using one of the Ag, Au or Cu fixed points. The measurement equation,

$$i_0 = \tau_{abs} \int S_{\mathrm{Re}\,l}(\lambda) \cdot L(\lambda, T_0) \cdot d\lambda \,, \tag{20}$$

is used to determine the absolute throughput. In Eq. 19, the photocurrent, i_0, is measured and the spectral radiance is known from the given temperature, T_o. Once the absolute throughput is determined, the radiation thermometer is used to measure the temperature of a blackbody using

$$i_1 = \tau_{abs} \int S_{\mathrm{Re}\,l}(\lambda) \cdot L(\lambda, T_1) \cdot d\lambda \,, \tag{21}$$

where i_1 is the measured photocurrent, and the temperature, T_1, can be determined by iteratively changing the integrand until the calculated photocurrents match the measured photocurrent.

5. Thermodynamic Temperature Measurements using Radiometric Techniques

The measurements of temperature can be classified into primary and secondary thermometry[51]. Primary thermometry is defined as determining thermodynamic temperatures using equations of state and physical constants without any adjustable temperature-dependent parameters. Since primary thermometers are not easily transportable and are difficult to use, secondary thermometers are used as transfer devices. Because of the difficulties in maintaining primary thermometers for routine calibrations, the International Temperature Scale of 1990 (ITS-90) assigns fixed values for the phase-transition temperatures of various pure materials based upon the best thermodynamic-temperature determinations available at the time of specifying the scale. Secondary interpolating thermometers are based upon these fixed points and the assigned temperatures are ultimately traceable to primary thermometers through the fixed points. Some examples of secondary thermometers are standard platinum resistance thermometers and thermocouples.

Another type of primary thermometer is the total and the spectral radiometer, calibrated using electrical substitution radiometry and used in conjunction with a blackbody. Such total radiometers in the past have determined the Stefan-Boltzmann constant using the wavelength integrated Planck's radiance law to a relative combined uncertainty of 0.013 %[52]. If only a narrow spectral region is selected by the use of spectral filters, then the spectral radiometer can be used to determine the temperatures of blackbodies with the use of Planck's radiation law within the spectrally selected region.

In the past, detector-based radiance temperature measurements have been performed using filter radiometers calibrated for spectral irradiance responsivity[53]. These filter radiometers with precision apertures are typically used in non-imaging applications to measure the temperatures of blackbodies, but such optical flux techniques are difficult to use to measure the fixed-point blackbodies with sub-centimeter diameter cavity openings. The non-imaging radiometers are used to measure spectral irradiance using double-aperture flux transfer techniques, and the small, < 1 cm internal apertures of fixed-point blackbodies make it difficult to define a source aperture. Such techniques can also result in large uncertainties in the diffraction corrections needed from the use of the small defining apertures. However, small aperture blackbodies can be measured using imaging radiometers in which the field-stop defines the area of measurement. In the past, absolute imaging radiometers or pyrometers have been constructed from filter radiometers using a lens with a measured transmittance [[54]], but similar component-based calibrations cannot be used with low final uncertainties if a number of optical elements such as lenses and filters are introduced into the optical path.

In this work, measurements of the thermodynamic temperatures of the Ag- and Au-freezing points using the NIST Absolute Pyrometer (AP1) are described in which the radiation thermometer is calibrated at the system level. The AP1 is designed and constructed at NIST and is calibrated for radiance responsivity as a system using a cryogenic, electrical-substitution radiometer-based method. The thermodynamic temperatures are compared to the previous temperature measurements and found to be in agreement within the combined uncertainties. This work demonstrates that the thermodynamic temperatures can be directly disseminated in this range using detector-based calibrations with comparable or lower uncertainties than that of ITS-90.

2.2 Radiance Responsivity Calibration of the AP1

The AP1 was calibrated for absolute radiance responsivity using the NIST Spectral Irradiance and Radiance responsivity Calibrations using Uniform Sources (SIRCUS) facility as illustrated in the sequence of measurements in Figs. 23a to 23d. The optical power of the power-stabilized and collimated laser source is measured using a cryogenic electrical substitution radiometer, the NIST Primary Optical Power Radiometer (POWR) in Fig. 23a. Since the POWR is difficult to use on a daily basis, the power responsivity is transferred to 6-element Si-trap detectors in Fig. 23b. From the knowledge of the spatial uniformity and the area of the precision, defining aperture on the trap detectors, the detector-based spectral irradiance responsivity is determined. The laser is input into an integrating sphere to obtain a spatially uniform and lambertian source in Fig. 23c and the spectral irradiance of the source is determined using the Si-trap detector. The spatial uniformity at the exit aperture of the integrating sphere is mapped to determine the uncertainties due to the non-uniformity of the sphere. The power-stabilized laser is transmitted through a fiber which is agitated in a water-filled ultrasonic bath. The rapid vibrations in the ultrasonic bath remove the laser speckle in the sphere output since the integration times of the detectors are much longer than the time duration of the speckle pattern. A small 38.1 mm diameter, integrating sphere is used to increase the throughput of the sphere and the 5 mm diameter exit port of the integrating sphere source is chosen to approximate the 6 mm diameter opening of the fixed-point blackbody cavities. With precision apertures on both the output port of the integrating sphere and the entrance of the Si-trap detector combined with the knowledge of the distance separating the sphere and the trap detector, the monochromatic spectral radiance of the integrating sphere can be assigned from the detector-calibrated irradiance responsivity of the trap detector. The aperture area and the distance measurement device are traceable to length standards. The AP1 is then calibrated for spectral radiance responsivity by substitution with the trap detector as shown in Fig. 23d. Once the monochromatic, spectral radiance of the integrating-sphere source is known, any radiometer or radiation thermometer can be calibrated at the system level. The procedure is repeated at other wavelengths until the full spectrum of the radiance responsivity is obtained.

The detector-based radiance responsivity of the AP1 is shown along with the spectral radiance of the gold-point blackbody in Fig. 24. The interference filter used in the AP1 shows > $1\text{x}10^{-7}$ suppression in the out-of-band region relative to the peak value of the responsivity. The full-width at half-maximum (FWHM) of the radiance responsivity is 10 nm, with the centroid wavelength of 649.115 nm. The total expanded uncertainty of the radiance responsivity at a single wavelength is 0.15 % ($k = 2$).

The wavelength spacing between calibrations was decreased near the peak of the spectral responsivity since interference effects from inter-reflections can lead to oscillations in the spectral responsivity which are wavelength dependent, as seen in Fig. 4. **WHERE IS THIS FIGURE ?** The sources of the interference effects are from the remaining coherence of the laser through the integrating sphere source combined with the inter-reflections between optical elements in the radiation thermometer. Although effort was made to reduce the interference effects by designing the optical filter with a 5° tilt of one of the surfaces from the optical axis, the interference effects are evident as < 1 % peak oscillations of the responsivity. Since the radiation thermometer is used to measure the radiance from a blackbody which is an incoherent source, the convolved radiance will not exhibit the interference effects, and the interference effects in the radiance responsivity will depend on the spatial coherence of the incident radiation. The increase in the uncertainties due to the interference effects can be minimized by performing measurements at closely spaced wavelength intervals.

The thermodynamic temperatures of blackbodies are found from the radiance responsivity and Planck's law by the use of

$$i_c = \int S_L \cdot L(\lambda, T) d\lambda \ , \tag{22}$$

where i_c is the calculated photocurrent, S_L is the absolute radiance responsivity, and $L(\lambda, T)$ is the spectral radiance given by the Planck radiance law. The Planck radiance law is

$$L(\lambda, T) = \frac{\mathrm{c}_{1\mathrm{L}}}{\mathrm{n}^2 \lambda^5} \frac{1}{\exp\left(\mathrm{c}_2 / (\mathrm{n} \lambda T)\right) - 1} \ , \tag{23}$$

where c_{1L} and c_2 are the first and second radiation constants , T is the thermodynamic temperature, λ is the wavelength of the radiation in air, and n is the refractive index. For these calculations, the CODATA values[55] for the radiation constants and the refractive index of air of n = 1.00029 were utilized.

There are no adjustable parameters in the measurement equation relating the radiance responsivity of the AP1 to the thermodynamic temperature, and Eq. 23 can be used to generate a curve of photocurrent to blackbody temperatures. The one-to-one relationship is shown in Fig. 25. The photodiode used in the AP1 is operated in the photovoltaic mode without any bias voltages, and this type of photodiode in the photovoltaic mode has been shown to be linear over a wide dynamic range[56]. The range of calculated photocurrents of the AP1 are from 1×10^{-11} A at the Ag-point to 1×10^{-6} A near 3000 K which is in the linear regime for photodiodes. The plot in Fig. 25 also indicates the need for low-noise current-to-voltage amplifiers to measure the low photocurrents near the Ag and Au freezing temperatures. Other corrections such as the size-of-source effect, non-linearity of the preamplifier and the emissivity of the blackbody will be applied as corrections to the measured photocurrents before comparison to the calculated photocurrents in Fig. 25. The relationship between photocurrent and blackbody temperatures can be fit with an interpolation function[57] to facilitate conversions from signals to temperatures.

2. Summary of systematic corrections to AP1

The correction factors listing the dominant systematic corrections to the AP1 signals are listed in Table 3. The AP1 signals were corrected prior to the application of Eq. 22 by using

$$i = G\frac{\sigma}{\varepsilon} i_m , \qquad (24)$$

where i_m is the measured photocurrent, i is the corrected photocurrent, G is the gain correction, ε is the emissivity, and σ is the SSE correction. The corrected photocurrent can then be directly compared to the calculated photocurrents in Fig. 25. The gain correction factor is the normalization factor of gain 10^{10} to gain 10^8 as shown in Table 1 since the responsivity calibrations were performed at gain 10^8 while the Ag- and Au-freezing temperatures were measured at gain 10^{10}. The SSE correction will have the effect of reducing the measured signal since the responsivity calibration was used with a 5 mm diameter opening of the integrating sphere source with no other source of radiation outside the opening. The emissivity of blackbodies will also reduce the radiance and thus compensation can be made using Eq. 24.

3. Discussion

The discussion of the uncertainties of the measurements must start from the initial uncertainties arising from the initial realization to the cryogenic electrical substitution radiometer in the NIST SIRCUS facility, and the component uncertainties are listed in Table 6. The component uncertainties arise from the individual transfers and step as shown in Fig. 2 **???**. The two largest components, line 4 and line 7, are due to the spatial uniformity and the uniformity of the angular output of the integrating sphere and the long-term stability of the trap detectors. Since the windows in the multi-element diode trap detectors are removed to avoid multiple reflections between the windows and the diode surfaces, the power responsivities of the diodes can change due to contamination or surface damage. The final total uncertainty leads to the uncertainties in Table 7. Additional information on the uncertainties in the detector-based realizations can be found in Ref. 13 **???**.

The individual uncertainties are listed in Table 7 as a percent of the signals and then converted to temperature uncertainties. The dominant contribution to the expanded temperature uncertainties is the uncertainty in the radiance responsivity of 0.15 % ($k = 2$). Since the center wavelength of the AP1 is in the wavelength and temperature region where the Wien approximation is applicable, the uncertainty of the temperature from the uncertainty of radiance is found from the derivative of the Wien approximation,

$$\frac{dL}{L} = \frac{c_2}{\lambda}\frac{dT}{T^2}, \tag{25}$$

where L is the radiance, λ is the centroid wavelength, T is the temperature and c_2 is the second radiation constant.

Our detector-based Ag- and Au-freezing temperatures are in agreement with the measurements of Fox et al. who also used a detector-based filter radiometer to measure the Ag- and Au-freezing temperatures to be 1235.009 K (± 0.088 K) and 1337.330 K (± 0.098 K) respectively[58]. The differences of our temperature determinations with the earlier results by Fox et al. are within the combined uncertainties. The gold freezing temperature is also in agreement with the detector-based measurements of Mielenz et al[59].

Our results are also in agreement with the ITS-90 temperatures. The ITS-90 temperature assignments of the respective freezing temperature are primarily from the ratio pyrometry work of Fischer and Jung[60] with radiance ratios taken from a lower temperature blackbody at 730 K. The thermodynamic temperature of the blackbody was assigned from two conflicting constant-volume gas thermometry measurements[61] with differences of 30 mK at 730 K. Since the difference could not be resolved at the assignments of the ITS-90 fixed points, a decision was made to compromise between the two results and agree upon a compromise of 15 mK at 730 K, or half the value of the 30 mK difference. Since the uncertainties in temperature increase as

$$\Delta T_a = \frac{T_a^2}{T_b^2}\Delta T_b\,, \tag{26}$$

where ΔT_a and ΔT_b are the uncertainties of the blackbody at temperatures T_a and T_b, the resulting thermodynamic temperature offset at 1337 K resulting from ratio pyrometry is expected to be 50 mK.

In addition to the thermodynamic temperature uncertainties, the uncertainties in realizing a temperature scale using fixed-points include uncertainties due to material purity, emissivity of the cavity, furnace-temperature uniformity and furnace operation. Even if the fixed-point is filled initially with ultra pure (99.999 %) metal, the metal in the blackbody can become contaminated due to operations at high temperatures, and any contamination will suppress the freezing temperature. To have reproducible and stable freeze plateaus, the furnace should have a uniform temperature distribution. The electrical power heating of the furnace has also to be optimized to achieve reproducible and flat freeze plateaus. The dependence of the freezing temperature on the impurities and the operational parameters can lead to realization uncertainties of 50 mK ($k = 2$)[62], and temperature scale comparisons can require side-by-side operation of the respective fixed-points to achieve lower temperature uncertainties.

The transition to detector-based radiance temperatures would lead to better agreement with thermodynamic temperatures and lead to direct dissemination of thermodynamic temperatures. This transition would be in accordance with the movement to having defined quantities or fixed values for the fundamental constants as the basis for the SI units instead of fixed artifacts as has already occurred for the candela in 1979. The dissemination of detector-based temperatures would also result in having a common basis, the electrical watt and length units, for photometric, radiometric and temperature scales possibly leading to resolution of any inconsistencies in the national scales. The uncertainties in the SIRCUS-based radiance responsivity calibrations are expected to be near 0.05 % ($k = 2$) in the near future with more frequent cryogenic radiometer realizations and finer wavelength intervals in the realized wavelengths. The resulting temperature uncertainty at the gold freezing temperatures from such improvements is expected to result in ~ 50 mK ($k = 2$) uncertainties.

Table 2: The calculated imaging performance of the lens combinations tested for SSE. The optical performance of the GRIN lens was not calculated due to the limitations of the modeling software.

Lens	**Focal Length [mm]**	**Diffraction Limited Radius [mm]**	**Geometric RMS Radius [mm]**	**Ratio Geometric/Diffraction Radii**	**Strehl Ratio**
PAC091-1 PAC091-2	500 500	0.00872	0.00122	0.14	0.990
PAC091-1 PAC089	500 300	0.00532	0.00211	0.40	0.921
PAC089	300	0.0107	0.0441	4.12	0.158
PAC088	250	0.00886	0.0504	5.69	0.112
PAC087	200	0.00589	0.0488	8.29	0.071

Table 3. The optical performance of the PAC088 lens at different wavelengths. The optical performance improves at longer wavelengths.

Wavelength [nm]	**Diffraction Limited Spot Radius [mm]**	**Geometric Spot Radius [mm]**	**Ratio Diffraction/Geometric Radii**	**Strehl Ratio**
900	0.0124	0.0527	4.25	0.144
1550	0.0219	0.0545	2.49	0.243
2250	0.0336	0.0556	1.65	0.310

Table 4. The lens parameters for the 1:1 imaging optimized lens with a focal length of 200 mm at 650 nm. The optimized lens is constructed using common achromat glass types.

Surface	**Radius of Curvature [mm]**	**Center Thickness [mm]**	**Material**
R_1	102.70	10.0	BK7
R_2	-73.52	4.0	SF5
R_3	-317.68	--	--

Table 5. Optical performance of the 1:1 optimized achromat lens from Table 4. The lens is found to be diffraction-limited in performance from 650 nm to 2250 nm. The lens performances are evaluated at the focus.

Wavelength [nm]	**Diffraction Limited Spot Diameter [mm]**	**Geometric Spot Diameter [mm]**	**Ratio Diffraction/Geometric Spot Diameters**	**Strehl Ratio**
650	0.00589	0.00598	1.02	0.808
900	0.00816	0.00601	0.74	0.791
1550	0.0144	0.00811	0.56	0.851
2250	0.0219	0.00684	0.31	0.955

Table 4. The gains and the photocurrents at the fixed-point temperatures measured using a variable-temperature blackbody set at the respective temperatures. The standard deviations of the photocurrents at the respective temperatures are converted to noise-equivalent temperature difference (NETD).

Fixed Point	**Temperature [°C]**	**Gain [V/A]**	**Signal [A]**	**NETD [°C]**
In	156.5985	10^{10}	2.26251E-11	0.0050
Sn	231.928	10^{9}	5.36748E-10	0.0011
Zn	419.527	10^{7}	7.45110E-08	0.0015
Al	660.323	10^{6}	2.23358E-06	0.0009
Ag	961.78	10^{5}	2.63766E-05	0.0013

Table 5. The gain ratios of the preamplifier measured using a 1 W white LED source with a Si detector.

Gains Compared	**Gain Ratios**	**Measurement Uncertainty (k = 2)**
$10^6/10^5$	9.998	0.002
$10^7/10^6$	10.001	0.002
$10^8/10^7$	10.000	0.002
$10^9/10^8$	10.000	0.002
$10^{10}/10^9$	9.957	0.002

Table 7. Table of standard uncertainty components listed according to their source. Items are stated in either temperature or in percents.

	Description	FPBB Scheme [%] (k=1)
Blackbody	Impurities	6.5 mK
	Plateau identification	10 mK
	Blackbody emissivity, isothermal	.02
	Cavity bottom heat exchange	35 mK
Radiation Thermometer (RT)	Size-of-source effect	.005
	Non-linearity	.002
	Atmospheric absorption	.01
	Gain ratios	.002
	Noise	.001
	Interpolation error	.03
RT Use	Drift	.05

Table 6. The thermodynamic temperature uncertainties for a total uncertainty of 0.05 % (k = 2) at the respective fixed-point temperatures.

Fixed Point	**Temperature [°C]**	**Total Uncertainty = 0.05% (k = 2) [K]**
In	156.5985	0.0099
Sn	231.928	0.0137
Zn	419.527	0.0258
Al	660.323	0.0469
Ag	961.78	0.0821

Table 2. Calculated emissivity of the graphite blackbody cavity with 50 mm depth and 57 ° conical bottom and λ = 650 nm with two different initial conditions for the graphite emissivity.

Aperture diameter [mm]	Emissivity with graphite emissivity, ε = 0.86	Emissivity with graphite emissivity, ε = 0.80
6.0	0.99964	0.99943
2.0	0.99996	0.99993
1.5	0.99998	0.99996
1.0	0.99999	0.99998

Table 3. Systematic correction factors to the AP1 signal.

Type of correction	**Gain, G**	**Emissivity, ε**	**SSE, σ**
Signal Correction Factor	1.0017	0.99964	0.99963
Uncertainty (k = 2)	0.022%	0.02%	0.02%

Table 6. The total uncertainty of the spectral radiance responsivity calibrations in the NIST SIRCUS facility broken down into the component uncertainties. Trap refers to the Si-diode trap detector used for the realization.

	SIRCUS Uncertainty Components (k=1)	Type	
1	Trap responsivity	B	0.025%
2	Aperture areas	B	0.004%
3	Distance	B	0.010%
4	Sphere Spatial and Angular Uniformity	B	0.050%
5	Amplifier gain	A	0.010%
6	Temperature coefficient of Trap	B	0.003%
7	Temporal Stability of Trap	B	0.050%
	Combined Standard Uncertainty (k=1)		0.076%
	Expanded Total Uncertainty (k=2)		**0.153%**

Table 7. Uncertainty components for the Ag and Au freezing temperature measurements.

	Signal uncertainty component [%] (*k*= 2)	**Ag**	**Au**
1	Spectral Radiance Responsivity	0.15	0.15
2	Temporal Stability of Responsivity	0.03	0.03
3	Plateau Identification	0.01	0.01
4	Emissivity	0.02	0.02
5	Non-linearity	0.022	0.022
6	Dark current drift	0.03	0.03
7	Size-of-source effect	0.02	0.02
	Total uncertainty in Signal	0.16	0.16
	Temperature uncertainty [K] (*k*=2)	**0.110**	**0.129**

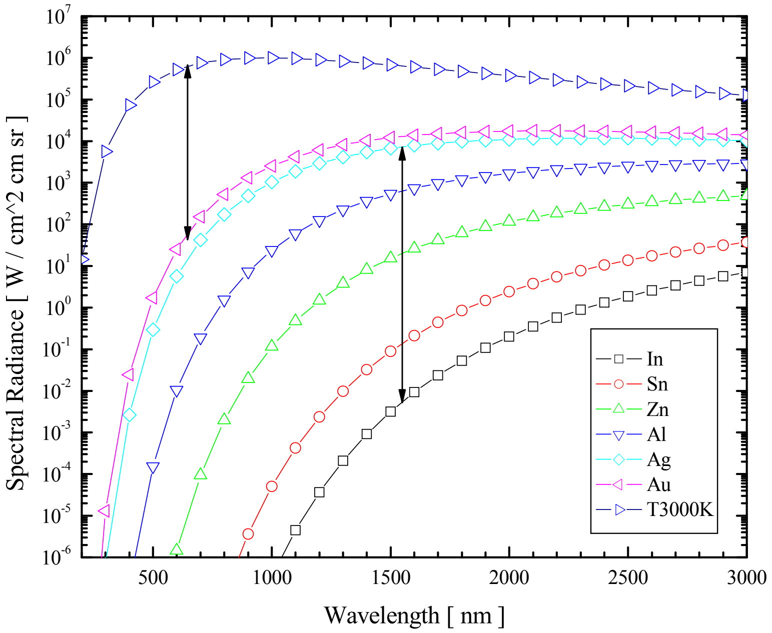

Fig. 1 The Planck radiances for blackbody temperature ranging from the freezing-point of In to 3000 K. The center wavelengths of commonly used radiation thermometers are indicated by the two lines at 650 nm and 1550 nm.

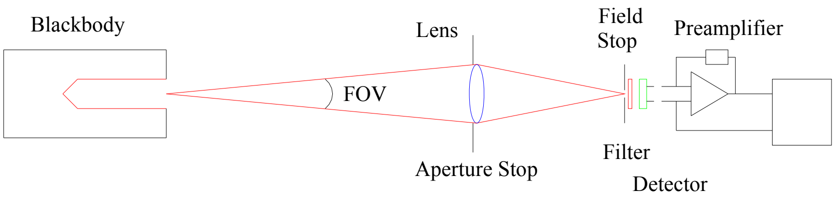

Figure 2. The schematic of a simple radiation thermometer showing the blackbody source, the objective lens, field stop, spectral filter, detector and the preamplifier. In this design, the aperture stop in front of the lens before the field stop.

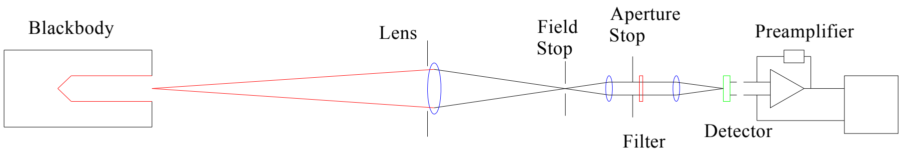

Figure 3. The schematic of a simple radiation thermometer with a Lyot stop showing the blackbody source, the objective lens, field stop, spectral filter, detector and the preamplifier. The aperture stop is behind the field stop to act as a Lyot stop.

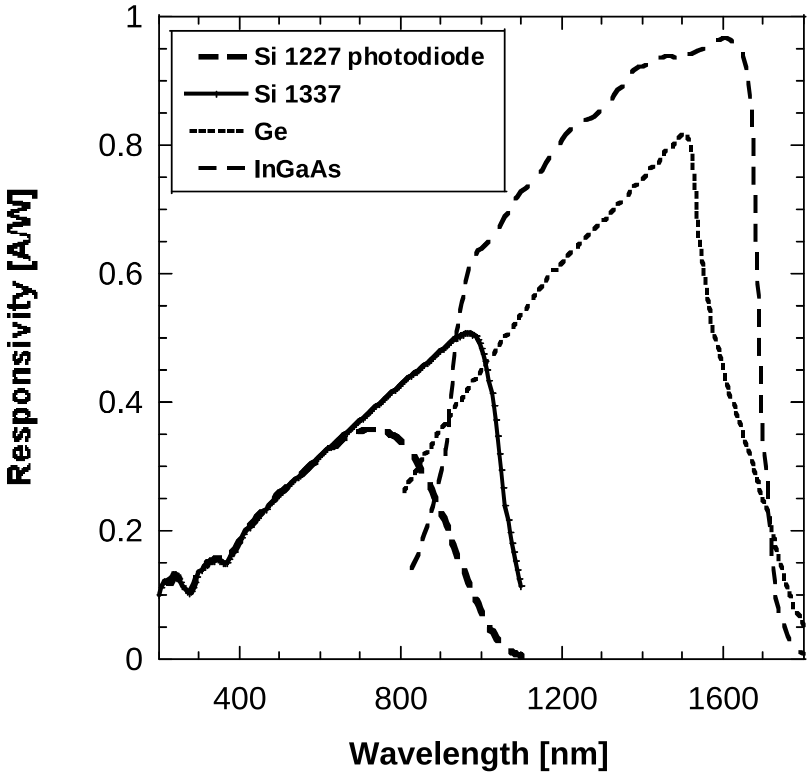

Fig. 4. Spectral power responsivities of frequently used detectors between 200 nm and 1800 nm.

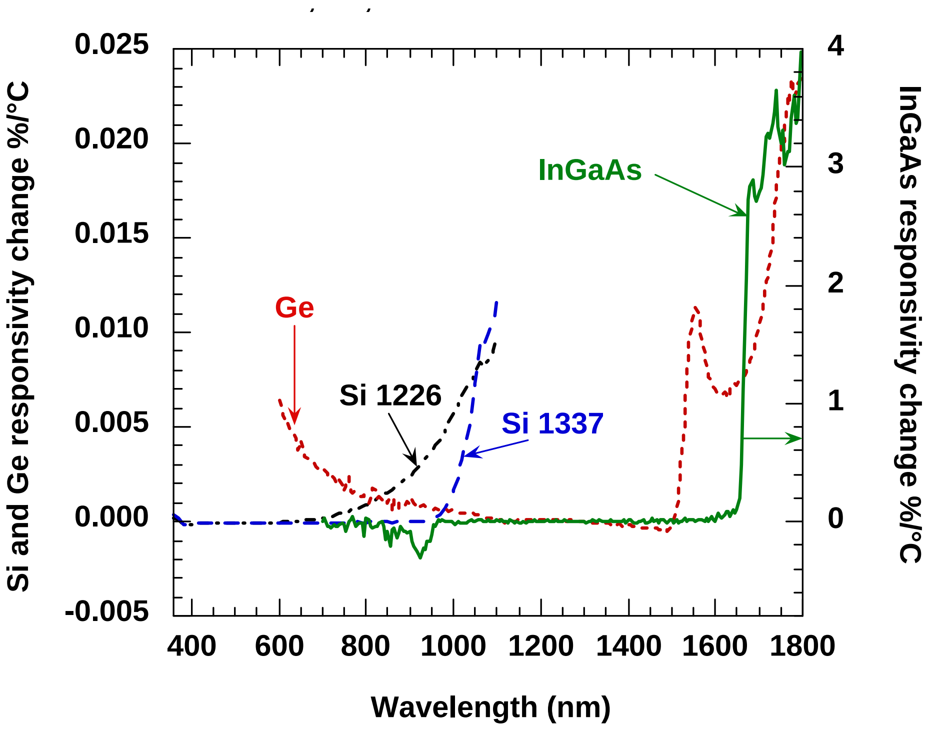

Fig. 5. The temperature dependent responsivities of the four popular photodiodes of Fig. 4

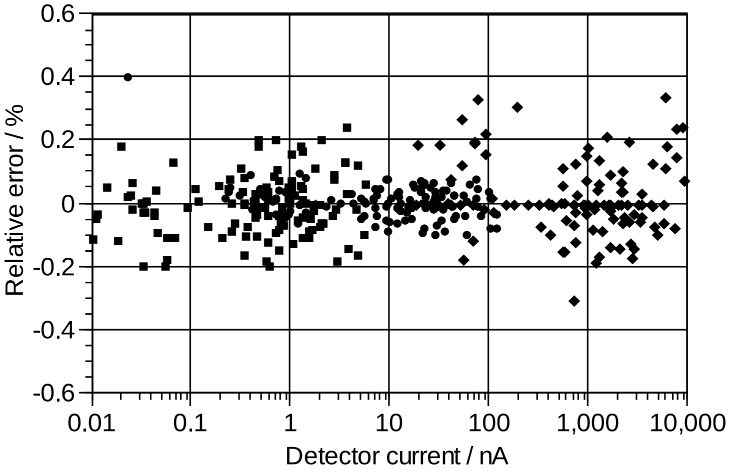

Figure 6: The non-linearity in a silicon detector determined using the combinatorial method. Three separate sets of 120 measurements are plotted.

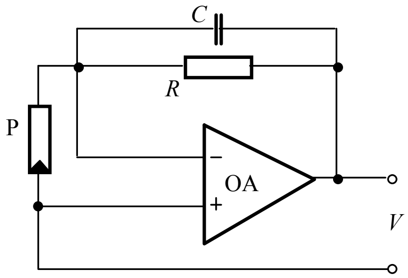

Fig. 7. Circuit diagram of a simple photocurrent meter.

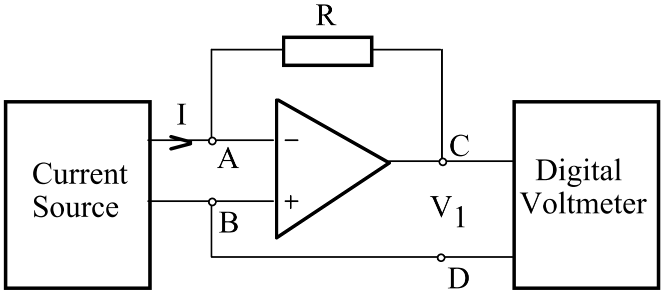

Figure 8. Current determination with the current-to-voltage converter standard.

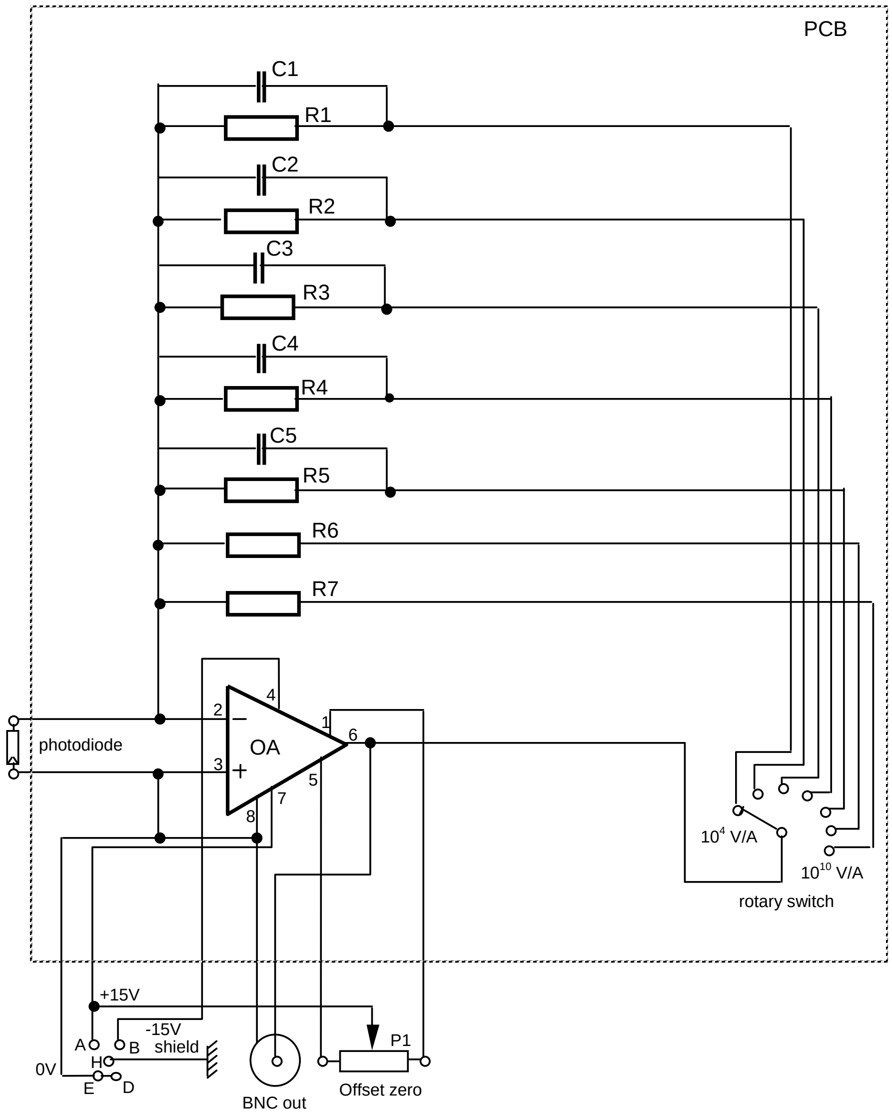

Figure 9. Circuit diagram of a simple photocurrent meter.

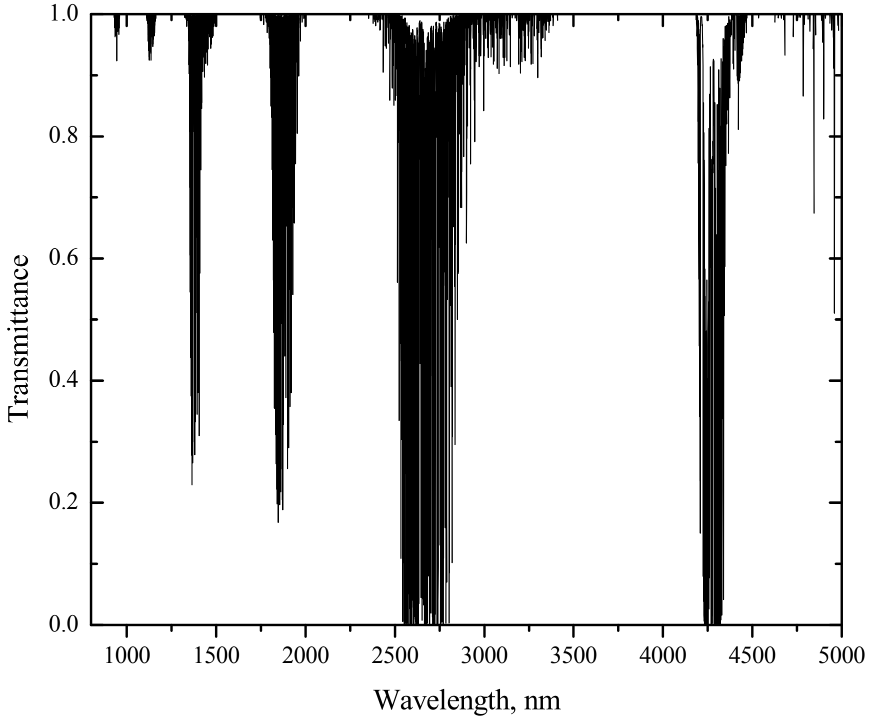

Fig. 10. The atmospheric transmittances for 1 m path at sea level and 296 K conditions.

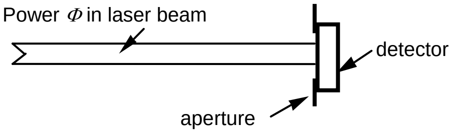

Fig.11. Measurement geometry of radiant power measurement.

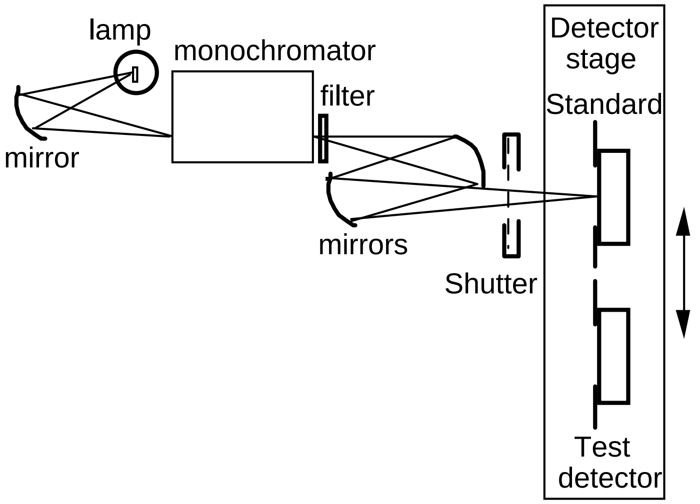

Fig. 12. Spectral responsivity measurement setup using a monochromator.

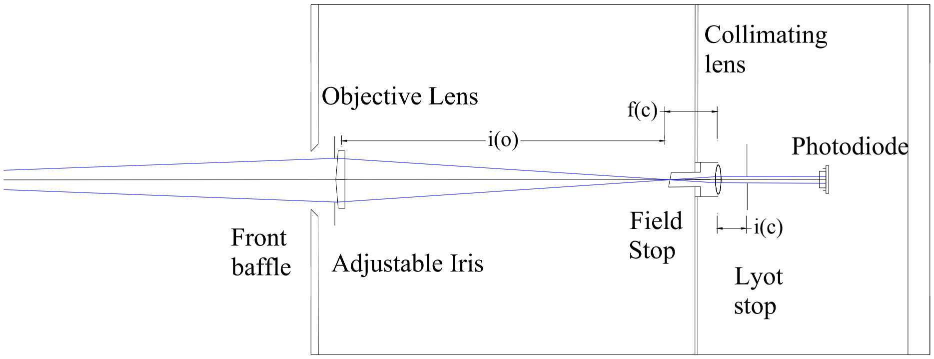

Figure 13. The schematic of the radiation thermometer used for the SSE measurements. The objective lens is placed on a V-groove mount for quick and reproducible changes of the lens.

?????

Fig. 14a. LED source

?????

Fig. 14b. Spectral radiance of LED source

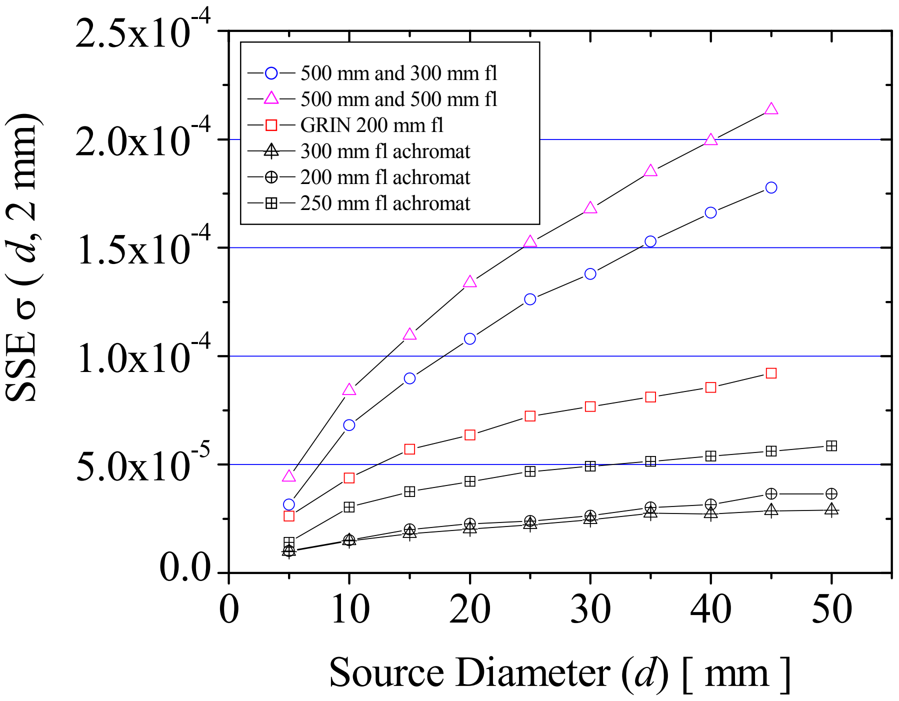

Figure 15. The measured SSE for different objective lenses. All the measurements were performed with the Lyot stop. The lenses with smaller number of elements have lower SSE from the reduced surfaces for scattering with a strong dependence on the surface finish.

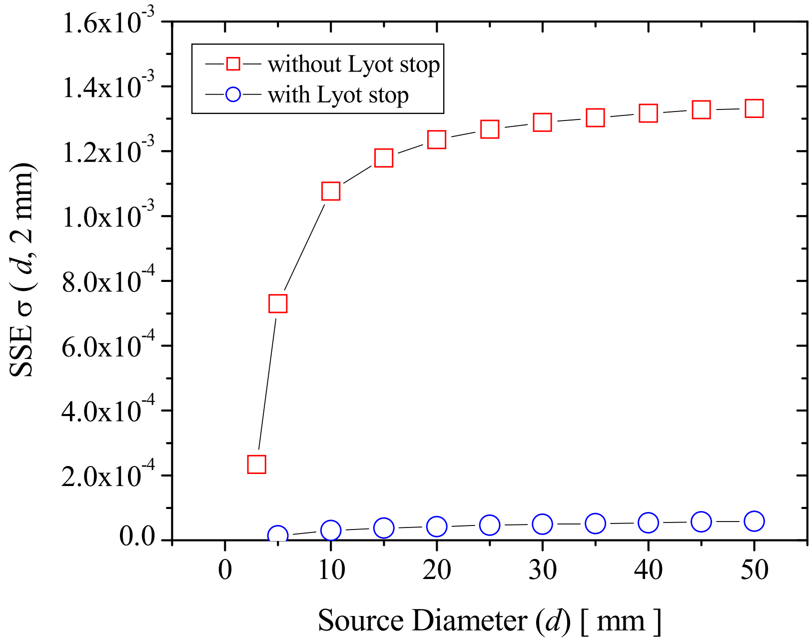

Figure 16. SSE comparison of 250 mm fl lens, PAC088, with and without the Lyot stop. The SSE increases by x 20 at 50 mm diameter without the Lyot stop.

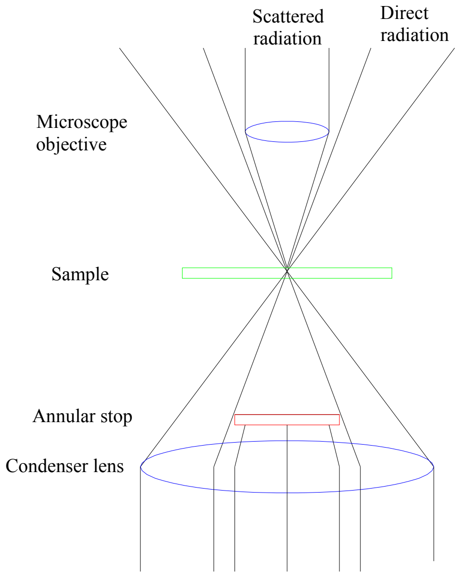

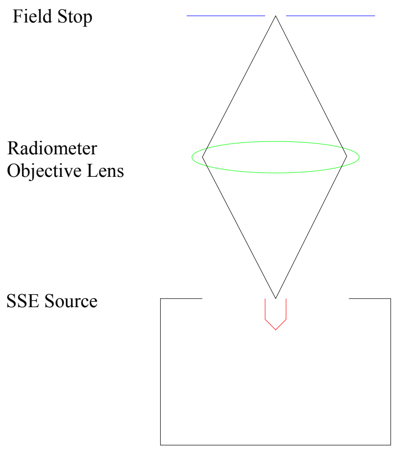

Figure 17a. Measurement schematic of dark-field microscopy. The situation is analogous to the "indirect" method of SSE determination with the objective lens as the sample and the source being the annular stop and the radiation from the condenser lens.

Figure 17b. Optical schematic of the SSE measurement. Only the scattered radiation is collected by the field stop showing that the SSE determinations measure the scattered transmittance of the objective lens.

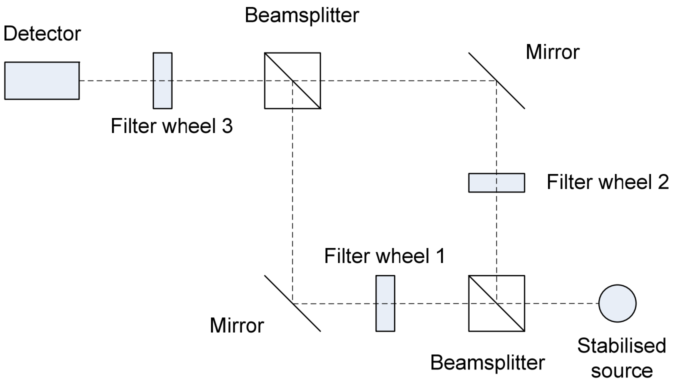

Figure 18: Simplified schematic diagram of the detector linearity testing facility.

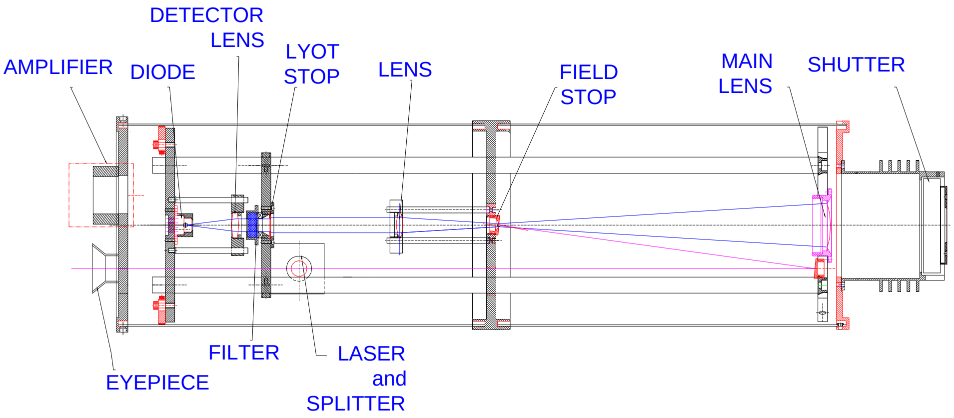

Fig. 19. The schematic of the InGaAs-based radiation thermometer with the optical components labeled. The outer diameter of the main body is 20.3 cm with a total length of 75 cm, excluding the front baffle. For alignment, the eyepiece is used to view the image on the tilted field stop. A laser can be made incident on the field stop for additional alignment.

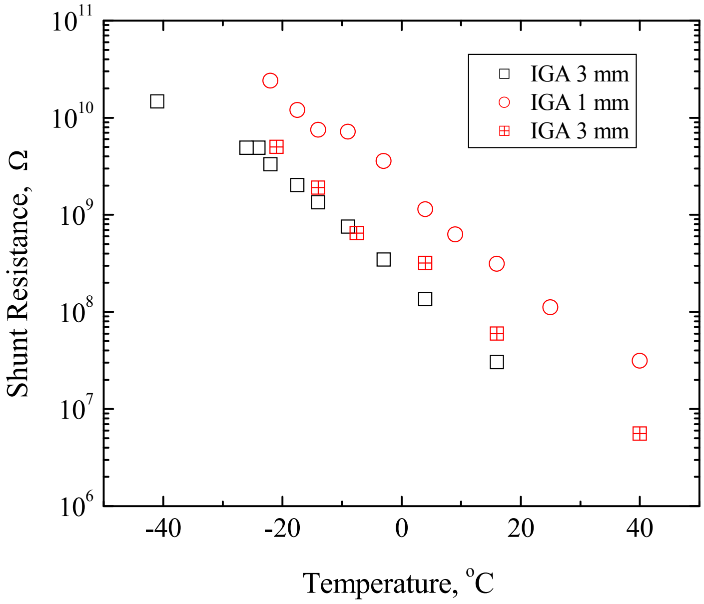

Fig. 20. The temperature-dependent shunt resistances of 1 mm and 3 mm diameter InGaAs (IGA) diodes. The shunt resistance of the diode should be comparable to the feedback resistance of the preamplifier circuit for low noise, linear operation.

Comment [KH1]: I understand the 3 mm and 1 mm nomenclature, but what is 3mm2 meant to imply? Also, there ought to be a space between the value and the unit in the legend.

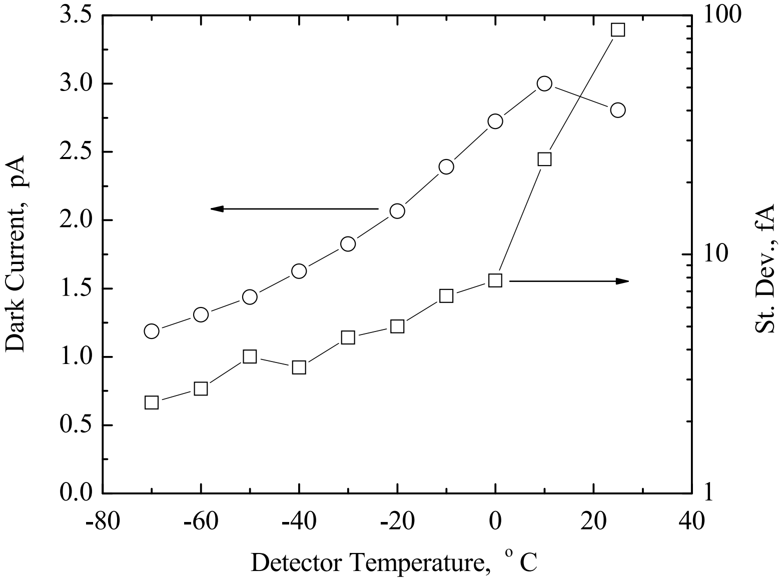

Fig. 21. The dark current (left axis) and the standard deviation (right axis) of the dark current measured with a bandwidth of 0.3 Hz as a function of the 3 mm diameter InGaAs detector temperature. The standard deviation of the dark current of the InGaAs detector at -70 °C nearly approaches Si-type detector performance.

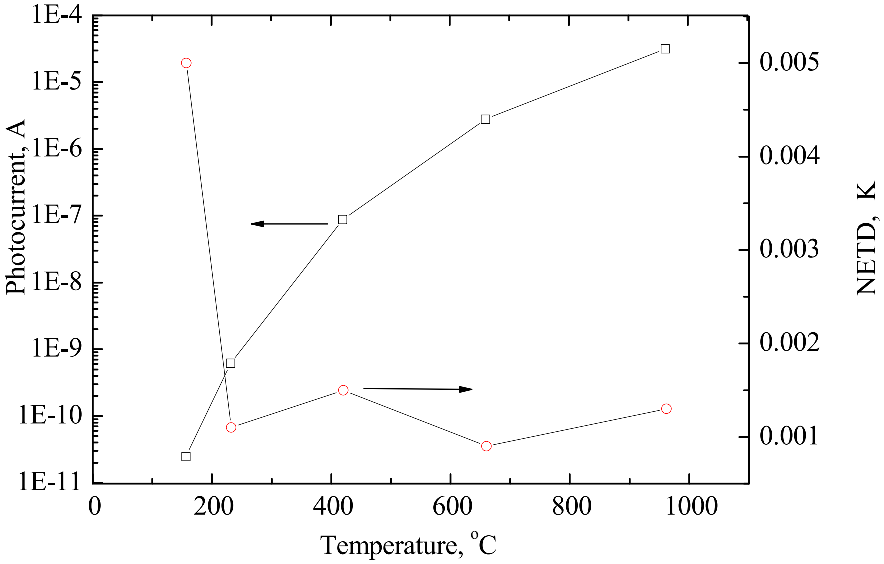

Fig. 22. The measured photocurrents of the InGaAs radiation thermometer at the various fixed point temperatures. The interpolations are performed using the photocurrent measurements. The NETD was determined from the standard deviation of the measurements.

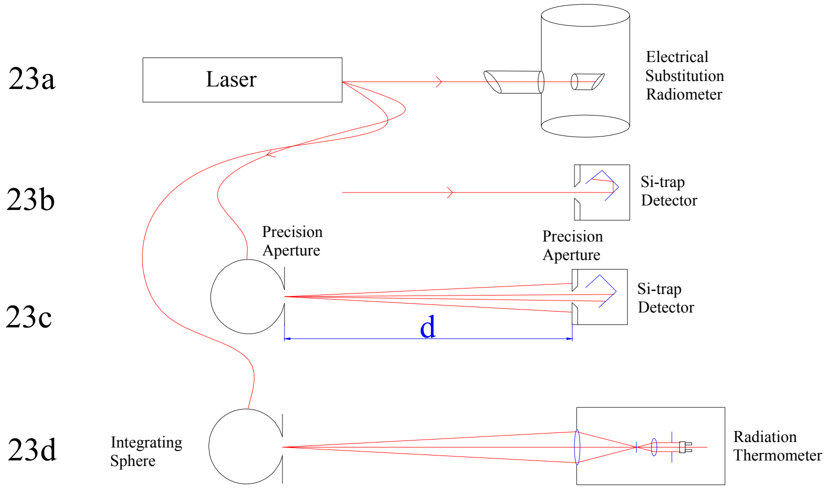

Figs 23a to 23d. The procedure for detector-based spectral radiance responsivity calibrations with the use of the electrical substitution radiometer. **23a.** Measurement of the spectral power of the laser with the cryogenic electrical substitution radiometer. **23b.** Determination of the spectral power responsivity of the Si-trap detector. **23c.** Measurement of the spectral irradiance of the integrating sphere source. **23d.** Determination of the radiance responsivity of the radiation thermometer as a system.

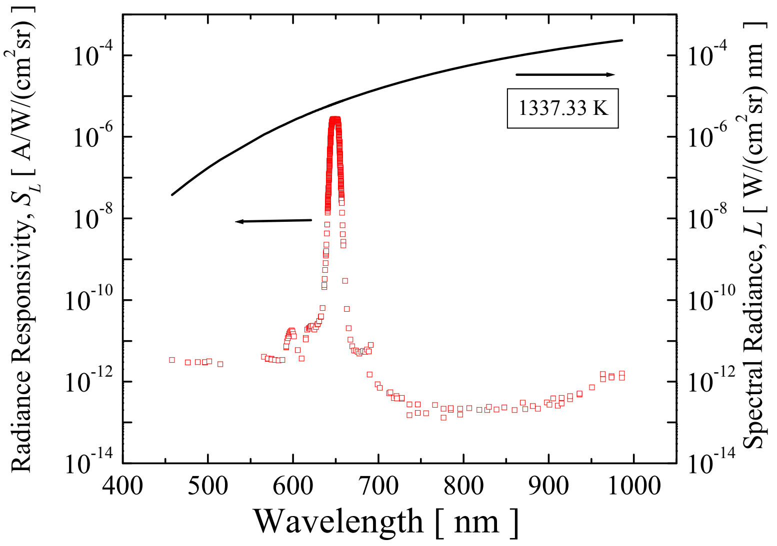

Figure 24. The radiance responsivity of the AP1 measured in the SIRCUS facility plotted with the Planck radiance at 1337.33 K. The center wavelength is 650 nm with a FWHM of 10 nm. The out-of-band suppression of < 1x10^{-7} is achieved in the wavelength region from 700 nm to 1000 nm.

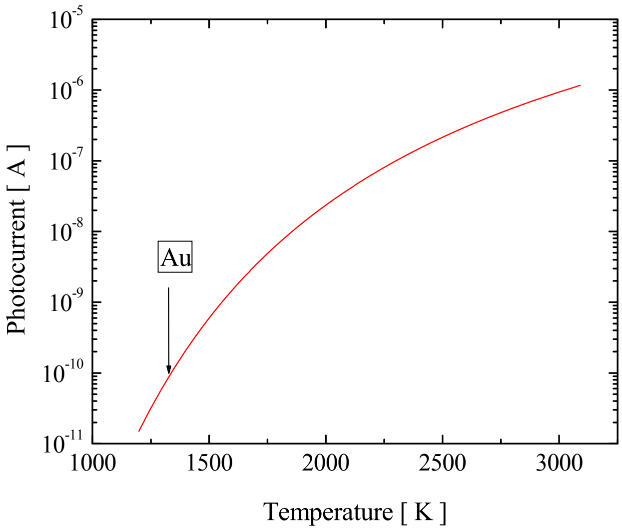

Figure 25. The calculated photocurrent as a function of the blackbody temperature. The calculation is performed with no adjustable parameters.

REFERENCES

* Certain commercial equipment, instruments, or materials are identified in this paper to foster understanding. Such identification does not imply recommendation or endorsement by the National Institute of Standards and Technology, nor does it imply that the material or equipment are necessarily the best available for the purpose.

[1] G. D. Nutter "Radiation Thermometers: Design Principles and Operating Characteristics," in *Theory and Practice of Radiation Thermometry*, edited by D. P. DeWitt and G. D. Nutter, Wiley, New York, pp. 91-187 (1988).

2 Preston-Thomas H., "The International Temperature Scale of 1990 (ITS-90)", Metrologia 27, 1990, pp. 3-10.

[3] J. Fischer, M. Battuello, M. Sadli, M. Ballico, S. N. Park, P. Saunders, Y. Zundong, B. C. Johnson, E. Van der Ham, F. Sakuma, G. Machin, N. Fox, W. Li, S. Ugur, and M. Matveyev, "Uncertainty Budgets for Realization of ITS-90 by Radiation Thermometry," in *Temperature: Its Measurement and Control in Science and Industry*, vol. 7, edited by D. C. Ripple, AIP, New York, pp. 631-638 (2003).

4 P. Saunders, J. Fischer, M. Sadli, M. Battuello, C. W. Park, Z. Yuan, H. Yoon, W. Li, E. van der Ham, F. Sakuma, J. Ishii, M. Ballico, G. Machin, N. Fox, J. Hollandt, M. Matveyev, P. Bloembergen, and S. Ugur, "Uncertainty Budgets for Calibration of Radiation Thermometers below the Silver Point," Int J Thermophys **29**, 1066–1083(2008).

[5] A. Thompson, and H.-M. Chen, "Beamcon III, a linearity measurement instrument for optical detectors," J. Res. NIST, 1994. **99**(6): p. 751-755.

[6] G. Eppeldauer, „Noise-optimized silicon radiometers,“ J. Res. Natl. Inst. Stand. Technol., 2000. **105**(No. 2): p. 209-219.

[7] NIST Technical Note 1438, *Optical Radiation Measurement with selected detectors and matched electronic circuits between 200 nm and 20 μm,* Editor: George P Eppeldauer, U.S. Government Printing Office, Washington, 2001.

[8] Put in our SPIE paper

[9]

[10] G. Eppeldauer, *Chopped Radiation Measurement With Large Area Si Photodiodes.* Journal of research at NIST, 1998. **103**: p. 153-162.

[11] G.,Eppeldauer, *Electronic characteristics of Ge and InGaAs radiometers.* SPIE proceedings, 1997. **3061**: p. 833-838.

[12] NIST Technical Note 1621, Optical radiation measurements based on detector standards, Editor: George P Eppeldauer, NIST Printing and Duplicating, Gaithersburg, MD, 2009.

[13] G. P. Eppeldauer, S. W. Brown, and K. R. Lykke, Chapter 4, Transfer standard filter radiometers: Applications to fundamental scales, p.155-211, Optical Radiometry, Vol. 41, Elsevier, 2005.

14 H. Takashashi, “Temperature Stability of Thin-film Narrow-bandpass Filters Produced by Ion-assisted Deposition,” Applied Optics **34**, 667-675 (1995).

15 C. E. Gibson, B. K. Tsai, A. C. Parr, “Radiance Temperature Calibrations,’ NIST Special Publication **250-43**, U.S. Governments Printing Office, Washington DC, 1998.

16 P., Bloembergen, Y. Duan, R. Bosma, and Z.Yuan, “The Characterization of Radiation Thermometers Subject to the Size-of-Source Effect,” in *Proceedings of TEMPEMKO 1996*, *6th Int.Symp. on Temperature and Thermal Measurements in Industry and Science*,

edited by P. Marcarino, Levrotto and Bella, Turin, pp. 261-266 (1997).

17 G. Machin, T. Ricolfi, M. Battuello, G. Negro, H.-J. Jung, P. Bloembergen, R. Bosma, J. Ivarsson, and T. Weckström, “Comparison of the ITS-90 Using a Transfer Standard Infrared Radiation Thermometer between Seven EU National Metrological Institutes,” Metrologia **33**, 197-206 (1996).

18 H. C. McEvoy, G. Machin, R. Friedrich, J. Hartmann, and J. Hollandt, “Comparison of the New NPL Primary Standard Ag Fixed-point Blackbody with the Primary Standard Fixed Point of PTB,”in *Temperature: Its Measurement and Control in Science and Industry*, vol. 7, edited by D. C. Ripple, AIP, New York, pp. 909-914 (2003).

19 T. Ricolfi, L. Wang, “Experiments and Remarks on the Size-of-Source Effect in Precision Radiation Thermometry,” *in Proc. TEMPMEKO 1993, 5th Int.Symp. on Temperature and Thermal Measurements in Industry and Science,* edited by ???, ???, Prague, pp.161-165 (1997).

20 G., Newkirk and D., Bohlin, “Reduction of Scattered Light in the Coronagraph,” Applied Optics **2**, 131-140 (1963).

21 B. Lyot, C. R. Acad. Sci. Paris **191**, p. 834 (1930).

22 G. Machin and R. Sergienko “A Comparative Study of Size-of-Source Effect Determination Techniques,” in *Proc. TEMPMEKO 2001, 8th Int.Symp. on Temperature and Thermal Measurements in Industry and Science*, edited by B. Fellmuth, J. Seidel, and G. Scholze, VDI Verlag, Berlin, pp. 155-160 (2002).

23 M. S. Matveyev, “New Method for Measuring the Size-of-source Effect in Standard Radiation Thermometry,” in *Proc. TEMPMEKO 2001, 8th Int.Symp. on Temperature and*

Thermal Measurements in Industry and Science, edited by B. Fellmuth, J. Seidel, and G. Scholze, VDI Verlag, Berlin, pp. 167-171 (2002).

24 P. Saunders and H. Edgar, **“**On the Characterization and Correction of the Size-of-source Effect in Radiation Thermometers,” Metrologia **46,** 62–74 (2009).

25 D. W. Allen, H. W. Yoon G. Dezsi, “Portable LED-Illuminated Radiance Source,” submitted to the *Proceedings of Tempmeko 2004*, Croatia, 2004.

26 D. Lowe, M. Battuello, G. Machin, and F. Girard, “A comparison of size-of-source effect measurements of radiation thermometers between IMGC and NPL,” *Proceedings of the 8th Temperature Symposium*, October 2002, Chicago, IL, ed. by D. C. Ripple, pp. 625-630.

27 *Optical Scattering: Measurement and Analysis*, John C. Stover, SPIE-The International Society for Optical Engineering, Bellingham, Washington, p.18 (1995).

28 P. Bloembergen and Y. Yamada, “The Impact of Size-of-source Effect on the Uncertainty of Fixed-point Radiance Temperatures: a Case Study,” in *Proceedings of TEMPEMKO 2004*, *9th Int.Symp. on Temperature and Thermal Measurements in Industry and Science*,, edited by D. Zvizdic, Laboratory for Process Measurement, Croatia, pp. 1141-1148 (2004).

[29] S Yang, I Vayshenker, X Li, and T R Scott, “Accurate determination of optical detector non-linearity”, *Proc. NCSL ’94*, Ed Pub, 353-362, 1994.

[30] L Coslovi and F Righini, "Fast Determination of the Nonlinearity of Photodetectors," Applied Optics **19**, 3200-3203 (1980).

[31] R D Saunders and J B Shumaker, “Automated radiometric linearity tester”, *Appl. Opt.*, **23**, 3504-3506, 1984.

[32] X Li, T R Scott, S Yang, C L Cromer, and M L Dowell,“Nonlinearity measurements of high-power laser detectors at NIST”, *J. Res. Natl. Inst. Stand. Technol.*, **109**, 429-434, 2004.

[33] D. K. Walker, K. J. Coakley, and J. D. Splett, “Non-linear modelling of tunnel diode detectors,” *Geoscience and Remote Sensing Symposium,* 2004 Proceedings, Vol.6, IEEE International, 3969-3972, 2004.

[34] P Saunders and D R White, “Propagation of uncertainty due to non-linearity in radiation thermometers,” Presented to TEMPMEKO 2007.

[35] K D Mielenz and K L Eckerle, “Spectrophotometer linearity testing using the double-aperture method,” Applied Optics **11**, 2294-2303 (1972).

[36] P Saunders and D R White, “Propagation of uncertainty due to non-linearity in radiation thermometers”, Presented to TEMPMEKO 2007.

[37] H W Yoon, J J Butler, T C Larasen and G P Eppeldauer, “Linearity of InGaAs diodes”, *Metrologia*, **40**, S154-S158, 2003.

38. T. Ricolfi, M. Battuello, F. Girard, G. Machin, H. McEvoy, S. Ugur, and A. Diril, "Radiation Temperature Sclaes between the Indium and Silver points realized at IMGC , NPL and UME using a fixed-point calibration technique," Meas. Sci. Technol. **13**, 2090- 2093 (2002).

39. F. Girard, and T. Ricolfi, "Analysis of Two Methods for Calibrating IR Thermometers in the Middle-temperature Range," in *Proceedings of TEMPEMKO 2004*, *9th Int.Symp. on Temperature and Thermal Measurements in Industry and Science*,, edited by D. Zvizdic, Laboratory for Process Measurement, Croatia, pp. 827-832 (2005).

40. T. Ricolfi, and F. Girard, "A Transfer Standard Infrared Thermometer for the Temperature Range 150 °C to 1000 °C," in *Proceedings of TEMPEMKO 1999*, *7th Int.Symp. on Temperature and Thermal Measurements in Industry and Science*, edited by J. F. Dubbledam and M. J. de Groot, Vol. II, IMEKO/ Nmi Van Swinden Laboratorium, Delft, The Netherlands, pp. 593 -598 (1999).

41. B. Gutschwager, S. Schiller, J. Hartmann, and J Hollandt, "A Lens-free InGaAs transfer Radiation Thermometer with an Extended Calibration Range above 960 °C," in *Proceedings of TEMPEMKO 2004*, *9th Int.Symp. on Temperature and Thermal Measurements in Industry and Science*,, edited by D. Zvizdic, Laboratory for Process Measurement, Croatia, pp. 605-610 (2005).

42. G. Romeo, and G. Frulla, Journal of Composite Materials **29**:751 (1995).

43. G. P. Eppeldauer, J. Res. Natl. Inst. Stand. Technol (U. S.) **105**:29 (2000).

44 F. Sakuma and M., Kobayashi in *Proceedings of TEMPEMKO 1996*, *6th Int.Symp. on Temperature and Thermal Measurements in Industry and Science*, edited by P. Marcarino, Levrotto and Bella, Turin, pp. 305-310 (1997).

45. H. W. Yoon, D. W. Allen, C. E. Gibson, M. Litorja, R. D. Saunders, S. W. Brown, G. P. Eppeldauer, K. R. Lykke, Applied Optics **46**: 2870 (2007).

[46] G. P. Eppeldauer, H. W. Yoon, Y. Zong, T. C. Larason, A. Smith, and M. Racz, "Absolute responsivity calibrations from 950 nm to 1650 nm with 0.05 % (*k*=2) uncertainty," accepted for publication in Metrologia (2009).

47. S. W. Brown, G. P. Eppeldauer, K. R. Lykke, "Facility for spectral irradiance and radiance responsivity calibrations using uniform sources," Applied Optics **45**, 8218-8237 (2006).

48 Supplementary Information for the International Temperature Scale of 1990, Sèvres, Bureau International des Poids et Mesures, 1990.

49 J. L. Gardner, "Effective Wavelength for Multicolor/pyrometry," Applied Optics **19**, pp. 3088-3091 (1980).

50 P. Saunders, "Uncertainty Arising from the Use of the Mean Effective Wavelength in Realizing ITS-90," in *Temperature: Its Measurement and Control in Science and Industry*, vol. 7, edited by D. C. Ripple, New York, AIP, 2003, pp. 639-644.

51. T. J. Quinn, *Temperature*, Academic Press, San Diego, 20-22 (1990).

52 T.J. Quinn and J. E. Martin, "A Radiometric Determination of the Stefan-Boltzmann Constant and Thermodynamic Temperatures between -40 °C and +100 °C," Phil. Trans. Roy. Soc. **316**, 85-189 (1985).

53 H. W. Yoon and C. E. Gibson, "Determination of Radiance Temperatures using Detectors Calibrated for Absolute Spectral Power Response," in *Proceedings of TEMPEMKO 1999*, *7th Int.Symp. on Temperature and Thermal Measurements in Industry and Science*, edited

by J. F. Dubbledam and M. J. de Groot, Vol. II, IMEKO/ Nmi Van Swinden Laboratorium, Delft, The Netherlands, 737-742 (1999).

54 N. P. Fox, J. E. Martin and D. H. Nettleton, "Radiometric Aspects of an Experiment to Determine the Melting/Freezing Temperature of Gold," *Metrologia* **28**, 221-227 (1991).

55 P. J. Mohr and B. N. Taylor, Rev. Mod. Phy. **77**, 1 (2005).

56 G. P. Eppeldauer and J. E. Hardis, " Fourteen-decade Photocurrent Measurements with Large-area Silicon Photodiodes at Room Temperature," Applied Optics **30**, 3091-3099 (1991).

57 F. Sakuma and S. Hattori, "Establishing a Practical Temperature Standard by using a Narrow-band Radiation Thermometer with a Silicon Detector," in *Temperature: Its Measurement and Control in Science and Industry*, vol. 5, edited by J. F. Schooley, AIP, New York, pp. 421-427 (1982).

58 N. P. Fox, J. E. Martin and D. H. Nettleton, "Absolute Spectral Radiometric Determinationof the Thermodynamic Temperatures of the Melting/Freezing Points of Gold, Silver and Aluminium," *Metrologia* **28**, 357-374 (1991).

59 K. D. Mielenz, R. D. Saunders and J. B. Shumaker, "Spectroradiometric Determination of the Freezing Temperature of Gold," J. Res. Natl. Inst. Stand. Technol. **95**, 49-67 (1990).

60 J. Fischer and H. J. Jung, "Determination of the Thermodynamic Temperatures of the Freezing Points of Silver and Gold by Near-Infrared Pyrometry," Metrologia **26**, 245-252 (1989).

61 R. L. Rusby, R. P. Hudson, M. Durieux, J. F. Schooley, P. P. M. Steur, C. A. Swenson, "Thermodynamic Basis of the ITS-90," Metrologia **28**, 9-18 (1991).

62 J. Fischer, M. Battuello, M. Sadli, M. Ballico, S. N. Park, P. Saunders, Y. Zundong, B. C. Johnson, E. Van der Ham, F. Sakuma, G. Machin, N. Fox, W. Li, S. Ugur, M. Matveyev, “Uncertainty Budgets for Realization of ITS-90 by Radiation Thermometry”, in *Temperature: Its Measurement and Control in Science and Industry*, vol. 7, edited by D. C. Ripple, New York, AIP, 2003, pp. 631-638.